



The Panchromatic Afterglow of GW170817: The Full Uniform Data Set, Modeling, Comparison with Previous Results, and Implications

S. Makhathini^{1,2,3} , K. P. Mooley^{4,5,34} , M. Brightman⁵ , K. Hotokezaka^{6,7} , A. J. Nayana^{8,9} , H. T. Intema¹⁰ , D. Dobie^{11,12,13} , E. Lenc¹² , D. A. Perley¹⁴ , C. Fremling¹⁵ , J. Moldòn^{16,17} , D. Lazzati¹⁸ , D. L. Kaplan¹⁹ , A. Balasubramanian²⁰ , I. S. Brown¹⁹ , D. Carbone²¹ , P. Chandra²² , A. Corsi²⁰ , F. Camilo² , A. Deller^{13,23} , D. A. Frail⁴ , T. Murphy^{11,13} , E. J. Murphy²⁴ , E. Nakar²⁵ , O. Smirnov^{1,2} , R. J. Beswick¹⁷ , R. Fender^{26,27} , G. Hallinan⁵ , I. Heywood^{1,2,28} , M. Kasliwal⁵ , B. Lee^{29,30} , W. Lu⁵ , J. Rana³¹ , S. Perkins² , S. V. White¹ , G. I. G. Józsa^{1,2,32} , B. Hugo^{1,2} , and P. Kamphuis³³

¹ Department of Physics & Electronics, Rhodes University, Makhanda, 6139, South Africa; sphemakh@gmail.com

² South African Radio Astronomy Observatory (SARAO), Observatory Road, Cape Town 7925, South Africa

³ School of Physics, University of the Witwatersrand, Johannesburg, Braamfontein, 2000, South Africa

⁴ National Radio Astronomy Observatory, Socorro, NM 87801, USA; kunal@astro.caltech.edu

⁵ Caltech, 1200 E. California Blvd. MC 249-17, Pasadena, CA 91125, USA

⁶ Department of Astrophysical Sciences, Princeton University, Peyton Hall, Princeton, NJ 08544, USA

⁷ Research Center for the Early Universe, Graduate School of Science, University of Tokyo, Bunkyo-ku, Tokyo 113-0033, Japan

⁸ Department of Physics, United Arab Emirates University, Al-Ain, 15551, UAE

⁹ National Centre for Radio Astrophysics, Tata Institute of Fundamental Research, P.O. Box 3, Pune, 411007, India

¹⁰ International Centre for Radio Astronomy Research, Curtin University, GPO Box U1987, Perth WA 6845, Australia

¹¹ Sydney Institute for Astronomy, School of Physics, University of Sydney, Sydney, New South Wales 2006, Australia

¹² ATNF, CSIRO Astronomy and Space Science, P.O. Box 76, Epping, New South Wales 1710, Australia

¹³ ARC Centre of Excellence for Gravitational Wave Discovery (OzGrav), Hawthorn, Victoria, Australia

¹⁴ Astrophysics Research Institute, Liverpool John Moores University, IC2, Liverpool Science Park, 146 Brownlow Hill, Liverpool L3 5RF, UK

¹⁵ Division of Physics, Mathematics and Astronomy, California Institute of Technology, Pasadena, CA 91125, USA

¹⁶ Instituto de Astrofísica de Andalucía (IAA, CSIC), Glorieta de las Astronomía, s/n, E-18008 Granada, Spain

¹⁷ Jodrell Bank Centre for Astrophysics, School of Physics and Astronomy, University of Manchester, Manchester M13 9PL, UK

¹⁸ Department of Physics, Oregon State University, 301 Weniger Hall, Corvallis, OR 97331, USA

¹⁹ Center for Gravitation, Cosmology, and Astrophysics, Department of Physics, University of Wisconsin-Milwaukee, P.O. Box 413, Milwaukee, WI 53201, USA

²⁰ Department of Physics and Astronomy, Texas Tech University, Box 1051, Lubbock, TX 79409-1051, USA

²¹ University of the Virgin Islands, 2 Brewers Bay Rd., Charlotte Amalie, USVI 00802, USA

²² National Centre for Radio Astrophysics, Tata Institute of Fundamental Research, Pune University Campus, Ganeshkhind Pune 411007, India

²³ Centre for Astrophysics & Supercomputing Swinburne University of Technology John St., Hawthorn VIC 3122, Australia

²⁴ National Radio Astronomy Observatory, Charlottesville, VA 22903, USA

²⁵ The Raymond and Beverly Sackler School of Physics and Astronomy, Tel Aviv University, Tel Aviv 69978, Israel

²⁶ Denys Wilkinson Building, Keble Rd., Oxford OX1 3RH, UK

²⁷ Department of Astronomy, University of Cape Town, Private Bag X3, Rondebosch 7701, South Africa

²⁸ Subdepartment of Astrophysics, Denys Wilkinson Building, Keble Rd., Oxford OX1 3RH, UK

²⁹ MS314-6, Infrared Processing and Analysis Center, California Institute of Technology, Pasadena, CA 91125, USA

³⁰ Korea Astronomy and Space Science Institute, Daedeokdae-ro 776, Yuseong-gu, Daejeon 34055, Republic of Korea

³¹ 104 Davey Lab, Box C-77, Penn State University, PA 16802, USA

³² Argelander-Institut für Astronomie, Auf dem Hügel 71, D-53121 Bonn, Germany

³³ Ruhr-Universität Bochum, Faculty of Physics and Astronomy, Astronomical Institute, D-44780 Bochum, Germany

Received 2020 June 3; revised 2021 August 13; accepted 2021 August 16; published 2021 November 26

Abstract

We present the full panchromatic afterglow light-curve data of GW170817, including new radio data as well as archival optical and X-ray data, between 0.5 and 940 days post-merger. By compiling all archival data and reprocessing a subset of it, we have evaluated the impact of differences in data processing or flux determination methods used by different groups and attempted to mitigate these differences to provide a more uniform data set. Simple power-law fits to the uniform afterglow light curve indicate a $t^{0.86 \pm 0.04}$ rise, a $t^{-1.92 \pm 0.12}$ decline, and a peak occurring at 155 ± 4 days. The afterglow is optically thin throughout its evolution, consistent with a single spectral index (-0.584 ± 0.002) across all epochs. This gives a precise and updated estimate of the electron power-law index, $p = 2.168 \pm 0.004$. By studying the diffuse X-ray emission from the host galaxy, we place a conservative upper limit on the hot ionized interstellar medium density, $< 0.01 \text{ cm}^{-3}$, consistent with previous afterglow studies. Using the late-time afterglow data we rule out any long-lived neutron star remnant having a magnetic field strength between $10^{10.4}$ and 10^{16} G. Our fits to the afterglow data using an analytical model that includes Very Long Baseline Interferometry proper motion from Mooley et al., and a structured jet model that ignores the proper motion, indicates that the proper-motion measurement needs to be considered when seeking an accurate estimate of the viewing angle.

Unified Astronomy Thesaurus concepts: Gravitational waves (678); Gravitational wave astronomy (675); High energy astrophysics (739); Neutron stars (1108); R-process (1324)

Supporting material: machine-readable table

³⁴ Jansky Fellow (NRAO/Caltech).

1. Introduction

Discovered on 2017 August 17 and localized to the lenticular galaxy NGC 4993 at 40 Mpc (Coulter et al. 2017), GW170817 is the first binary neutron star merger detected in gravitational waves (Abbott et al. 2017a). Uniquely, GW170817 was also accompanied by radiation across the electromagnetic spectrum (Abbott et al. 2017b), which allowed the merger astrophysics to be studied in great detail. A low-luminosity short γ -ray burst (SGRB; Goldstein et al. 2017; Savchenko et al. 2017) was observed 1.7 s after the merger. The macronova/kilonova, which peaked at ultraviolet (infrared) wavelengths on timescales of a few hours (days), indicated $\sim 0.05 M_{\odot}$ of r-process enriched merger ejecta traveling at $0.1c$ – $0.3c$ (e.g., Arcavi et al. 2017; Cowperthwaite et al. 2017; Drout et al. 2017; Kasen et al. 2017; Kasliwal et al. 2017; Nicholl et al. 2017; Pian et al. 2017; Smartt et al. 2017; Soares-Santos et al. 2017; Tanvir et al. 2017; Valenti et al. 2017; Villar et al. 2017).

The synchrotron afterglow, first detected 9 days after the merger at X-ray wavelengths (Troja et al. 2017), 16 days post-merger in the radio (Hallinan et al. 2017), and 110 days post-merger in the optical (Lyman et al. 2018), gave key insights into the relativistic ejecta and the circum-merger environment. The delayed onset and rising light curve of the afterglow ruled out an on-axis (typical) SGRB jet (Alexander et al. 2017; Evans et al. 2017; Haggard et al. 2017; Hallinan et al. 2017; Kim et al. 2017; Margutti et al. 2017; Murguia-Berthier et al. 2017; Troja et al. 2017; Lazzati et al. 2018; Lyman et al. 2018; Resmi et al. 2018; Ruan et al. 2018). Radio monitoring over the first 100 days after merger ruled out a simple (top-hat) off-axis jet and established that the panchromatic afterglow emission, as well as the γ -rays, were produced in a mildly relativistic wide-angle outflow (Mooley et al. 2018c). Such an outflow could be explained by a cocoon (e.g., Lazzati et al. 2017; Gottlieb et al. 2018) formed due to the interaction between an ultrarelativistic jet (as seen in SGRBs) and the merger dynamical/wind ejecta or due to the fast tail of the (fairly isotropic) dynamical ejecta. The afterglow emission peaked and started to decline approximately 160 days post-merger (Alexander et al. 2018; D’Avanzo et al. 2018; Dobie et al. 2018; Nynka et al. 2018; Troja et al. 2018). While the steeply declining light curve disfavored the isotropic ejecta model, the light curve and polarization measurements remained inconclusive as to whether a putative jet successfully penetrated the merger ejecta or was completely choked by it (e.g., Alexander et al. 2018; Corsi et al. 2018; Lamb et al. 2018; Margutti et al. 2018; Nakar & Piran 2018).

The degeneracy between the successful- and choked-jet models (e.g., Gill & Granot 2018; Nakar et al. 2018) was finally broken through the measurement of superluminal motion, at four times the speed of light between 75 and 230 days post-merger, of the radio source using Very Long Baseline Interferometry (VLBI; Mooley et al. 2018a). The light curve and VLBI modeling (Mooley et al. 2018a) together indicated that the jet core was successful and narrow, having an opening angle of $< 5^{\circ}$ and observed from a viewing angle between 14° and 28° , and energetic, with an isotropic equivalent energy of about 10^{52} erg (lying at the tail end of the regular SGRB distribution; Fong et al. 2015). The implied Lorentz factor close to the light-curve peak is $\Gamma \simeq 4$ (Mooley et al. 2018a). The strong constraints on the geometry of GW170817 facilitated a precise measurement of the Hubble constant (Hotokezaka et al. 2019). Subsequently, independent VLBI and afterglow light-curve observations (Fong et al. 2019;

Ghirlanda et al. 2019; Hajela et al. 2019; Lamb et al. 2019; Mooley et al. 2018b; Troja et al. 2019) confirmed the presence of a successful jet in the late-time afterglow of GW170817.

The wealth of observational data collected for the afterglow of GW170817 makes this one of the best studied (off-axis) SGRB afterglows. However, the data set currently available in the literature lacks uniformity, i.e., it suffers from differences in data processing and flux determination methods used by different groups. Recently, Fong et al. (2019) and Hajela et al. (2019) presented the reprocessing of some of the optical and X-ray afterglow data (Hubble Space Telescope or HST F606W 600 nm data and Chandra X-ray Observatory soft X-ray data), but the majority of the data (including radio data) were still lacking uniformity. Further, various groups have modeled the afterglow data of GW170817, but these groups have used different subsets of the data. The impact of these inhomogeneities is seen (at least partially) in the significant differences in the modeling results (e.g., Mooley et al. 2018a; Resmi et al. 2018; Ghirlanda et al. 2019; Lamb et al. 2019; Wu & MacFadyen 2019, see below). Taken together, a thorough compilation of all of the observational data and a uniform data set for the afterglow of GW170817 is warranted.

In this work we present a thorough compilation of the available radio, X-ray, and optical data. The work includes new data not published before, and a reprocessing of some previous data sets using consistent methodology. The result is a fairly uniform panchromatic data set of GW170817’s afterglow. The observational data span 0.5 to 940 days post-merger. We have made these afterglow measurements available in ASCII format on the web,³⁵ and this online data set will be continuously updated (beyond 940 days) as new measurements become available. The new observations, data compilation, and (re) processing are presented in Section 2. The full uniform afterglow data are presented in Table 2 and the light curve is shown in Figure 1. Section 3 describes power-law fits to the afterglow light curve and an analytical model to obtain jet and interstellar medium (ISM) parameters. Constraints on the density of the circum-merger environment and the nature of the merger remnant are presented in Section 4. In Section 5 we present preliminary fits to the afterglow light curve using the numerical structured jet model from Lazzati et al. (2018), a short review of all previous modeling efforts, and an examination of our modeling results in the context of previous results. We end with a summary and discussion in Section 6.

2. Data Compilation, (Re)Processing, and Analysis

We compiled all flux density upper limits from the literature (see references given in Table 2). Flux densities in the case of radio afterglow detections were compiled from Mooley et al. (2018b) and references therein, and optical (HST/F606W) afterglow detections were reported in the Fong et al. (2019) reprocessing. Below we report on new data obtained with the Karl G. Jansky Very Large Array (VLA), MeerKAT, the Australia Telescope Compact Array (ATCA), and *enhanced* Multi Element Remotely Linked Interferometer Network (eMERLIN) radio telescopes between 180 and 780 days post-merger spanning frequencies between 1.2 and 9 GHz.

We further reprocessed and analyzed radio data reported by Resmi et al. (2018), Margutti et al. (2018), and Alexander et al. (2018), ensuring a consistent method of flux determination (as

³⁵ <https://github.com/kmooley/GW170817/> or <http://www.tauceti.caltech.edu/kunal/GW170817/>.

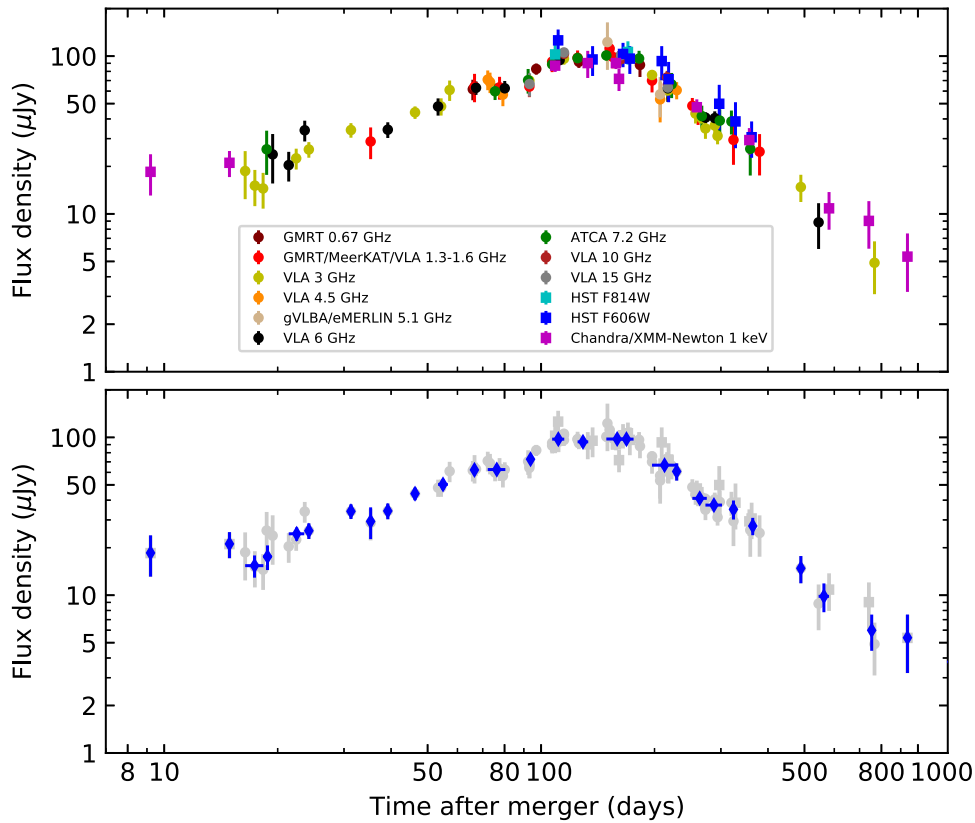


Figure 1. Upper panel: the panchromatic (radio, optical, and X-ray) afterglow light curve of GW170817, color coded according to the observing frequency, up to 940 days post-merger (all data points have 1σ error bars as presented in Table 2; upper limits are not shown here) using the uniform data set presented in this work. The light curve is scaled to 3 GHz using the best-fit spectral index (-0.584) derived from the Markov Chain Monte Carlo power-law fitting (see Section 3). Lower panel: the averaged (using the moving average; $\Delta t/t = 1/15$ where Δt is the width of the kernel and t is the time after merger) light curve (blue data points) shows a general trend consistent with a power-law rise and decline. In gray are the same data points as shown in the upper panel.

Table 1

Positions, Peak Flux Densities (Mean and Standard Deviations; $\mu\text{Jy beam}^{-1}$) at 0.7, 1.3, 3, 6, 7.2, 10, and 15 GHz for the Two Reference Sources used to Bootstrap the Flux Scale of the Radio Data Processed in This Work

R.A.	Decl.	$F_{0.7}$	$F_{1.3}$	F_3	F_6	$F_{7.2}$	F_{10}	F_{15}
$13^{\text{h}}09^{\text{m}}53^{\text{s}}.9$	$23^{\circ}21'34''$	530 ± 10	910 ± 20	565 ± 15	280 ± 10	300 ± 30	160 ± 5	70 ± 10
$13^{\text{h}}09^{\text{m}}44^{\text{s}}.5$	$23^{\circ}24'09''$	440 ± 20	230 ± 15	120 ± 10	65 ± 5	70 ± 10	60 ± 5	37 ± 5

reported in Mooley et al. (2018b). Similarly, we also reprocessed X-ray and optical (HST/F814W) data to ensure a uniform data processing and flux determination technique. Our radio reprocessing substantially improves the precision of the flux density values (by up to a factor of 2 in rms noise, i.e., the 1σ error bar) with respect to previously published values. Through our reprocessing, we find discrepancies of up to 1.5σ in the previously published radio flux density values. Our measurements with the reprocessed X-ray and optical data are in agreement, within 1σ , with previously published values.

The new observations and data (re)processing methods are described below, and the full afterglow data set spanning radio, optical, and X-ray frequencies is given in Table 2. We note that, in Table 2, all flux density measurements are quoted with 1σ error bars and all upper limits are 3σ . The full uniform afterglow light curve is shown in Figure 1.

2.1. VLA

VLA data of GW170817 covering the period between 2017 August 18 and 2018 January 8 have been reported by

Alexander et al. (2017), Hallinan et al. (2017), Mooley et al. (2018a, 2018b, 2018c), Margutti et al. (2018), and Alexander et al. (2018); see Table 2. We have reprocessed some of these observations (see Table 2) using the NRAO Common Astronomy Software Applications (CASA) pipeline (McMullin et al. 2007; version 5.4) and WSClean (Offringa et al. 2014) for imaging.³⁶

Additionally, we observed GW170817 on 2018 December 18–20 and 2019 September 24–27 with the VLA (PI: Corsi; VLA/18B-204). The Wideband Interferometric Digital Architecture (WIDAR) correlator was used at S band (2–4 GHz). We used PKS J1248–1959 as the phase calibrator and 3C 286 as

³⁶ Although we used WSClean, we noted that unresolved background radio sources in the field did not vary significantly with respect to the images generated using CASAClean (which was used for all other VLA data), thus ensuring uniformity of flux measurements for all VLA data. In order to quantify the imaging differences between the two software, we reimaged a few calibrated data sets with both WSClean and CASAClean, keeping the imaging parameters similar to the ones we used for the other reprocessed data sets. We found the mean flux density difference of sources within the FWHM of the primary beam to be $<2\%$.

Table 2
Radio Afterglow Measurements of GW170817

UT Date	ΔT^\dagger (days)	Telescope	ν (GHz)	F_ν (μ Jy)	σ_ν (μ Jy)	Reproc?	Original References
2017 Aug 18.10	0.57	VLA	9.7	<144	...	N	Alexander et al. (2017)
2017 Aug 18.21	0.68	ATCA	8.5	<120	...	N	Hallinan et al. (2017)
2017 Aug 18.21	0.68	ATCA	10.5	<150	...	N	Hallinan et al. (2017)
2017 Aug 18.46	0.93	uGMRT	0.61	<195	...	N	Hallinan et al. (2017)
2017 Aug 18.95	1.43	ALMA	338.5	<126	...	N	Kim et al. (2017)
2017 Aug 18.97	1.44	VLA	10.0	<13.8	...	N	Alexander et al. (2017)
2017 Aug 18.97	1.44	VLITE ^a /VLA	0.34	<34,800	...	N	Hallinan et al. (2017)
2017 Aug 19.95	2.41	ALMA	97.5	<75	...	N	Alexander et al. (2017)
2017 Aug 19.95	2.42	VLA	15.0	<17.7	...	N	Alexander et al. (2017)
2017 Aug 19.95	2.43	VLA	6.2	<20	...	N	Hallinan et al. (2017)
2017 Aug 19.95	2.43	VLA	9.7	<17	...	N	Hallinan et al. (2017)
2017 Aug 19.95	2.43	VLA	15	<22	...	N	Hallinan et al. (2017)
2017 Sep 19.97	2.44	VLITE/VLA	0.34	<28,000	...	N	Hallinan et al. (2017)
2017 Aug 19.97	2.44	VLA	10.0	<17.1	...	N	Alexander et al. (2017)
2017 Aug 19.97	2.46	VLA	6.0	<21.9	...	N	Alexander et al. (2017)
2017 Aug 20.31	2.78	uGMRT	0.4	<780	...	N	Hallinan et al. (2017)
2017 Aug 20.46	2.93	uGMRT	1.2	<98	...	N	Hallinan et al. (2017)
2017 Aug 20.76	3.23	ALMA	338.5	<90	...	N	Kim et al. (2017)
2017 Aug 20.87	3.34	VLA	3	<32	...	N	Hallinan et al. (2017)
2017 Aug 20.87	3.34	VLITE/VLA	0.34	<44,700	...	N	Hallinan et al. (2017)
2017 Aug 21.23	3.67	ATCA	8.5	<135	...	N	Hallinan et al. (2017)
2017 Aug 21.23	3.67	ATCA	10.5	<99	...	N	Hallinan et al. (2017)
2017 Aug 23.0	5.48	VLA	10.0	<28.5	...	N	Alexander et al. (2017)
2017 Aug 25.4	7.9	uGMRT	1.39	<69	...	N	Kim et al. (2017)
2017 Aug 25.8	8.29	VLA	10.0	<17.4	...	N	Alexander et al. (2017)
2017 Aug 25.96	8.37	VLITE/VLA	0.34	<37,500	...	N	Hallinan et al. (2017)
2017 Aug 25.96	8.43	ALMA	338.5	<150	...	N	Kim et al. (2017)
2017 Aug 26.96	9.43	ALMA	338.5	<102	...	N	Kim et al. (2017)
2017 Aug 27.00	9.43	ALMA	97.5	<72	...	N	Alexander et al. (2017)
2017 Aug 28.2	10.6	ATCA	8.5	<54	...	N	Hallinan et al. (2017)
2017 Aug 28.2	10.6	ATCA	10.5	<39	...	N	Hallinan et al. (2017)
2017 Aug 29.5	11.9	uGMRT	0.7	<123	...	N	Hallinan et al. (2017)
2017 Aug 30.9	13.4	VLA	10.0	<18.3	...	N	Alexander et al. (2017)
2017 Aug 31.0	13.5	VLITE/VLA	0.34	<20,400	...	N	Hallinan et al. (2017)
2017 Aug 31.0	13.5	VLA	6.2	<17	...	Y	Hallinan et al. (2017)
2017 Aug 31.5	13.9	uGMRT	0.4	<600	...	N	Hallinan et al. (2017)
2017 Sep 1.8	15.3	ALMA	97.5	<39	...	N	Alexander et al. (2017)
2017 Sep 1.9	15.4	VLA	6.2	<13	...	N	Hallinan et al. (2017)

Table 2
(Continued)

UT Date	ΔT^\dagger (days)	Telescope	ν (GHz)	F_ν (μ Jy)	σ_ν (μ Jy)	Reproc?	Original References
2017 Sep 1.9	15.4	VLITE/VLA	0.34	<11,400	...	N	Hallinan et al. (2017)
2017 Sep 2.9	16.4	VLITE/VLA	0.34	<11,700	...	N	Hallinan et al. (2017)
2017 Sep 2.9	16.4	VLA	3	18.7	6.3	N	Hallinan et al. (2017)
2017 Sep 3.0	16.5	VLA	6.2	<15	...	Y	Hallinan et al. (2017)
2017 Sep 3.9	17.4	VLA	3	15.1	3.9	N	Hallinan et al. (2017)
2017 Sep 3.9	17.4	VLITE/VLA	0.34	<6900	...	N	Hallinan et al. (2017)
2017 Sep 4.0	17.5	VLA	6.2	<15	This work
2017 Sep 4.9	18.3	VLA	3	14.5	3.7	N	Hallinan et al. (2017)
2017 Sep 5.2	18.7	ATCA	7.25	15.4	4.8	Y	Hallinan et al. (2017), Mooley et al. (2018b)
2017 Sep 5.5	19.0	uGMRT	0.7	<140	...	N	Hallinan et al. (2017)
2017 Sep 5.9	19.4	VLA	6.2	15.9	5.5	N	Hallinan et al. (2017)
2017 Sep 5.9	19.4	VLA	10.0	<13.5	...	N	Alexander et al. (2017)
2017 Sep 5.9	19.4	VLA	6.0	19	6	N	Alexander et al. (2017)
2017 Sep 6.0	19.5	VLA	10	<14	This work
2017 Sep 7.9	21.4	VLITE/VLA	0.34	<8100	...	N	Hallinan et al. (2017)
2017 Sep 7.9	21.4	VLA	6.2	13.6	2.9	N	Hallinan et al. (2017)
2017 Sep 8.9	22.4	VLA	3	22.5	3.4	N	Hallinan et al. (2017)
2017 Sep 8.9	22.4	VLITE/VLA	0.34	<6300	...	N	Hallinan et al. (2017)
2017 Sep 9.4	23.0	uGMRT	1.39	<108	...	N	Kim et al. (2017)
2017 Sep 9.9	23.4	VLITE/VLA	0.34	<4800	...	N	Hallinan et al. (2017)
2017 Sep 9.9	23.4	VLA	6	22.6	3.4	Y	Hallinan et al. (2017)
2017 Sep 10.8	24.2	VLA	3	25.6	2.9	N	Hallinan et al. (2017)
2017 Sep 10.9	24.3	VLITE/VLA	0.34	<6600	...	N	Hallinan et al. (2017)
2017 Sep 16.3	29.8	uGMRT	1.39	<126	...	N	Kim et al. (2017)
2017 Sep 16.3	29.7	uGMRT	0.68	<246	...	N	Mooley et al. (2018c)
2017 Sep 16.9	30.3	ALMA	97.5	<42	...	N	Alexander et al. (2017)
2017 Sep 17.8	31.3	VLA	3	34	3.6	N	Mooley et al. (2018c)
2017 Sep 21.9	35.3	VLA	1.5	44	10	N	Mooley et al. (2018c)
2017	36.9	VLA	1.6	<40	...	N	Mooley et al. (2018a)
Sep 23–24							
2017 Sep 25.8	39.2	VLA	6	22.8	2.6	Y	Alexander et al. (2017)
2017 Sep 26.0	39.4	VLA	15	<18	This work
2017 Sep 30.0	44.1	ALMA	338.5	<93	...	N	Kim et al. (2017)
2017 Oct 2.8	46.3	VLA	3	44	4	N	Mooley et al. (2018c)
2017 Oct 7–8	51.5	VLA	3.2	<60	...	N	Mooley et al. (2018a)
2017 Oct 9.8	53.3	VLA	6	32	4	N	Mooley et al. (2018c)
2017 Oct 10.8	54.3	VLA	3	48	6	N	Mooley et al. (2018c)
2017 Oct 13.7	57.2	VLA	3	61	9	N	Mooley et al. (2018c)
2017	65.9	uGMRT	0.67	148	22	Y	Mooley et al. (2018c)
Oct 20–26							
2017 Oct 23.3	66.6	uGMRT	1.3	98	20	Y	Resmi et al. (2018)
2017 Oct 23.7	67.2	VLA	6	42.6	4.1	N	Mooley et al. (2018c)
2017 Oct 28–	72.2	VLA	4.5	58	5	N	Mooley et al. (2018a)
Nov 4							
2017 Nov 1.0	75.5	ATCA	7.35	35.9	4.3	N	Mooley et al. (2018b, 2018c)
2017 Nov 3.1	77.6	uGMRT	1.4	97	16	Y	Resmi et al. (2018)
2017 Nov 4.7	79.2	VLA	4.5	45	7	N	Mooley et al. (2018a)
2017 Nov 5.7	80.1	VLA	6	41.7	4.7	...	This work
2017 Nov 17.9	92.4	ATCA	7.25	31.7	4.3	N	Dobie et al. (2018), Mooley et al. (2018b)
2017 Nov 17.9	75.5	ATCA	7.35	39.6	7	N	Mooley et al. (2018c)
2017 Nov 18.6	93.1	VLA	1.5	98	14	N	Mooley et al. (2018c)
2017 Nov 18.6	93.1	VLA	3	70	5.7	N	Mooley et al. (2018c)
2017 Nov 18.7	93.2	VLA	15	26	4.4	Y	Mooley et al. (2018c)
2017	97.1	uGMRT	0.67	199	16	Y	Resmi et al. (2018)
Nov 20–27							
2017 Dec 2	107	uGMRT	1.3	141	20	Y	Resmi et al. (2018)
2017 Dec 2	107	ATCA	1.3	53.2	4.5	N	Mooley et al. (2018b)
2017 Dec 7	112	VLA	6	62.9	3.2	Y	Margutti et al. (2018)
2017 Dec 10	115	VLA	3	96.2	8	Y	Margutti et al. (2018)
2017 Dec 10	115	VLA	10	51.2	3.4	Y	Margutti et al. (2018)
2017 Dec 10	115	VLA	15	41.2	1.9	Y	Margutti et al. (2018)
2017 Dec 20	125	ATCA	7.25	58.2	5	N	Dobie et al. (2018), Mooley et al. (2018b)

Table 2
(Continued)

UT Date	ΔT^\dagger (days)	Telescope	ν (GHz)	F_ν (μ Jy)	σ_ν (μ Jy)	Reproc?	Original References
2017 Dec 20	125	uGMRT	1.3	149	17	Y	Resmi et al. (2018)
2017 Dec 21	126	uGMRT	0.67	221	19	Y	Resmi et al. (2018)
2017 Dec 25– Jan 2	134	LOFAR	0.114	<6300	...	N	Broderick et al. (2020)
2018 Jan 13	149	ATCA	7.25	60.6	4.3	N	Dobie et al. (2018), Mooley et al. (2018b)
2018 Jan 14	150	eMERLIN	5.1	90	30	...	This work
2018 Jan 16	152	uGMRT	1.3	171	18	Y	Resmi et al. (2018)
2018 Jan 20	155	MeerKAT	1.3	151	23	...	This work
2018 Jan 27	163	VLA	3	97.3	11.3	Y	Margutti et al. (2018)
2018 Jan 27	163	VLA	6	67.3	4.1	Y	Margutti et al. (2018)
2018 Jan 27	163	VLA	10	47.4	3.6	Y	Margutti et al. (2018)
2018 Jan 27	163	VLA	15	39.6	2	Y	Margutti et al. (2018)
2018 Feb 1	167	ATCA	7.25	57.9	6.9	N	Dobie et al. (2018), Mooley et al. (2018b)
2018 Feb 17	183	uGMRT	0.65	211	34	N	Mooley et al. (2018b)
2018 Feb 13–28	187	eMERLIN	5.1	<83	This work
2018 Mar 2	197	VLA	3	75.9	5.2	N	Dobie et al. (2018)
2018 Mar 3	197	MeerKAT	1.3	107	17	Y	Mooley et al. (2018b)
2018 Mar 1–6	198	eMERLIN	5.1	<90	This work
2018 Mar 12–13	207	gVLBA	5	42	12	N	Ghirlanda et al. (2019)
2018 Mar 8–22	210	eMERLIN	5.2	<60	...	N	Ghirlanda et al. (2019)
2018 Mar 21	216	VLA	10	36.3	3.6	N	Mooley et al. (2018b)
2018 Mar 22	217	VLA	3	60.5	7.5	Y	Alexander et al. (2018)
2018 Mar 22	217	VLA	6	41.7	7.5	Y	Alexander et al. (2018)
2018 Mar 22	217	VLA	10	32.6	4	Y	Alexander et al. (2018)
2018 Mar 22	217	VLA	15	24.7	3.1	Y	Alexander et al. (2018)
2018 Mar 25–26	218	VLA	3	64.7	2.7	N	Mooley et al. (2018b)
2018 Mar 27	222	ATCA	7.25	39.7	7.2	N	Mooley et al. (2018b)
2018 Apr 1–10	229	VLA	4.5	48	6	N	Mooley et al. (2018a)
2018 Apr 26	252	MeerKAT	1.3	74	9	...	This work
2018 May 1	257	VLA	3	43.2	5.8	Y	Alexander et al. (2018)
2018 May 6	261	MeerKAT	1.3	66	10	...	This work
2018 May 11–12	267	ATCA	7.25	25	4.1	N	Mooley et al. (2018b)
2018 May 12	267	VLA	3	40.3	2.7	N	Mooley et al. (2018b)
2018 May 17	273	VLA	3	34.8	4.9	Y	Alexander et al. (2018)
2018 May 17	273	VLA	6	27.2	2.1	Y	Alexander et al. (2018)
2018 May 13–25	275	uGMRT	0.65	<153	...	N	Mooley et al. (2018b)
2018 Jun 2	289	VLA	3	36.3	3.9	Y	Alexander et al. (2018)
2018 Jun 2	289	VLA	6	27	2.8	Y	Alexander et al. (2018)
2018 Jun 7	294	VLA	3	31.2	3.6	N	Mooley et al. (2018b)
2018 Jun 11	298	ATCA	7.25	23.4	4.2	N	Mooley et al. (2018b)
2018 Jul 4	320	ATCA	7.25	23.1	4.0	Y	Troja et al. (2019)
2018 Jul 8	324	MeerKAT	1.3	47.2	12.8	...	This work
2018 Aug 12	359	ATCA	7.25	15.5	5.0	Y	Troja et al. (2019)
2018 Aug 23–26	372	LOFAR	0.114	<18,600	...	N	Broderick et al. (2020)
2018 Sep 2	380	MeerKAT	1.3	37.9	11.1	...	This work
2018 Sep 13	391	ATCA	7.25	<13	...	Y	Troja et al. (2019)
2018 Nov 21	461	ATCA	7.25	<11	This work
2018 Dec 18–20	489	VLA	3	14.8	2.9	...	This work
2019 Dec 20– Jan 3	496	MeerKAT	1.3	<22	This work
2019 Jan 14	515	ATCA	7.25	<13	This work
2019 Jan 21– Mar 29	545	VLA	6	5.9	1.9	N	Hajela et al. (2019)
2019 Mar 19	580	ATCA	7.25	<18	This work (PI: Piro)
2019 Aug 11–30	734	VLA	6	<8.4	...	N	Hajela et al. (2019)

Table 2
(Continued)

UT Date	ΔT^\dagger (days)	Telescope	ν (GHz)	F_ν (μJy)	σ_ν (μJy)	Reproc?	Original References
2019 Sep 16	760	ATCA	7.25	<13	This work
2019 Sep 21–27	767	VLA	3	4.9	1.8	...	This work
X-ray measurements							
2017 Aug 18.1	0.6	Swift	2.41×10^8	$<7.8 \times 10^{-3}$...	N	Evans et al. (2017)
2017 Aug 18.2	0.7	NuSTAR	1.20×10^9	$<7.3 \times 10^{-4}$...	N	Evans et al. (2017)
2017 Aug 18.5	1.0	Swift	2.41×10^8	$<7.5 \times 10^{-2}$...	N	Evans et al. (2017)
2017 Aug 18.6	1.1	Swift	2.41×10^8	$<5.0 \times 10^{-3}$...	N	Evans et al. (2017)
2017 Aug 19.0	1.5	Swift	2.41×10^8	$<3.7 \times 10^{-3}$...	N	Evans et al. (2017)
2017 Aug 19.6	2.1	Swift	2.41×10^8	$<2.9 \times 10^{-3}$...	N	Evans et al. (2017)
2017 Aug 19.8	2.3	Swift	2.41×10^8	$<3.8 \times 10^{-3}$...	N	Evans et al. (2017)
2017 Aug 19.9	2.4	Chandra	2.41×10^8	$<2.24 \times 10^{-4}$...	N	Margutti et al. (2017), Troja et al. (2017), Nynka et al. (2018)
2017 Aug 20.1	2.6	Swift	2.41×10^8	$<4.0 \times 10^{-3}$...	N	Evans et al. (2017)
2017 Aug 20.4	2.9	Swift	2.41×10^8	$<1.1 \times 10^{-3}$...	N	Evans et al. (2017)
2017 Aug 21.1	3.6	Swift	2.41×10^8	$<1.9 \times 10^{-3}$...	N	Evans et al. (2017)
2017 Aug 21.9	4.4	NuSTAR	1.20×10^9	$<5.8 \times 10^{-4}$...	N	Evans et al. (2017)
2017 Aug 22.0	4.5	Swift	2.41×10^8	$<1.8 \times 10^{-3}$...	N	Evans et al. (2017)
2017 Aug 23.3	5.8	Swift	2.41×10^8	$<2.0 \times 10^{-3}$...	N	Evans et al. (2017)
2017 Aug 24.0	6.5	Swift	2.41×10^8	$<2.2 \times 10^{-3}$...	N	Evans et al. (2017)
2017 Aug 26.7	9.2	Chandra	2.41×10^8	4.48×10^{-4}	$+1.44_{-1.19} \times 10^{-4}$	Y	Troja et al. (2017), Margutti et al. (2017), Nynka et al. (2018), Hajela et al. (2019)
2017 Aug 27.0	9.5	Swift	2.41×10^8	$<2.5 \times 10^{-3}$...	N	Evans et al. (2017)
2017 Aug 28.4	10.9	Swift	2.41×10^8	$<4.0 \times 10^{-3}$...	N	Evans et al. (2017)
2017 Aug 29.0	11.5	Swift	2.41×10^8	$<1.7 \times 10^{-3}$...	N	Evans et al. (2017)
2017 Aug 30.0	12.5	Swift	2.41×10^8	$<1.6 \times 10^{-3}$...	N	Evans et al. (2017)
2017 Aug 31.1	13.6	Swift	2.41×10^8	$<1.1 \times 10^{-3}$...	N	Evans et al. (2017)
2017 Sep 01.2	14.7	Swift	2.41×10^8	$<1.3 \times 10^{-3}$...	N	Evans et al. (2017)
2017 Sep 01.4	14.9	Chandra	2.41×10^8	5.11×10^{-4}	$+1.02_{-0.90} \times 10^{-4}$	Y	Troja et al. (2017), Margutti et al. (2017), Haggard et al. (2017), Nynka et al. (2018), Hajela et al. (2019)
2017 Sep 02.4	15.9	Swift	2.41×10^8	$<4.3 \times 10^{-3}$...	N	Evans et al. (2017)
2017 Sep 04.7	18.2	NuSTAR	1.20×10^9	$<1.8 \times 10^{-3}$...	N	Evans et al. (2017)
2017 Sep 05.6	19.1	NuSTAR	1.20×10^9	$<1.2 \times 10^{-3}$...	N	Evans et al. (2017)
2017 Sep 06.7	20.2	NuSTAR	1.20×10^9	$<9.2 \times 10^{-4}$...	N	Evans et al. (2017)
2017 Sep 21.5	35.0	NuSTAR	1.20×10^9	$<4.6 \times 10^{-4}$...	N	Evans et al. (2017)
2017 Nov 28	103	NuSTAR	1×10^9	$<2.6 \times 10^{-3}$...	N	Troja et al. (2018)
2017 Nov 28	103	NuSTAR	3×10^9	$<2.0 \times 10^{-3}$...	N	Troja et al. (2018)
2017 Dec 4	109	Chandra	2.41×10^8	21.17×10^{-4}	$+1.90_{-1.80} \times 10^{-4}$	Y	Ruan et al. (2018), Margutti et al. (2018), Troja et al. (2018), Nynka et al. (2018)
2017 Dec 29	133	XMM-Newton	2.41×10^8	21.94×10^{-4}	$+4.42_{-4.15} \times 10^{-4}$	Y	D’Avanzo et al. (2018)
2018 Jan 23	158	Chandra	2.41×10^8	21.87×10^{-4}	$+1.88_{-1.78} \times 10^{-4}$	Y	Troja et al. (2018), Margutti et al. (2018), Nynka et al. (2018)
2018 Jan 26	161	XMM-Newton	2.41×10^8	17.38×10^{-4}	$+2.89_{-2.76} \times 10^{-4}$	Y	Piro et al. (2019)
2018 May 4	259	Chandra	2.41×10^8	11.50×10^{-4}	$+1.45_{-1.34} \times 10^{-4}$	Y	Nynka et al. (2018), Piro et al. (2019), Hajela et al. (2019)
2018 Aug 10	357	Chandra	2.41×10^8	7.12×10^{-4}	$+1.45_{-1.27} \times 10^{-4}$	Y	Troja et al. (2019), Hajela et al. (2019)
2019 Mar 22	581	Chandra	2.41×10^8	2.63×10^{-4}	$+0.77_{-0.64} \times 10^{-4}$	Y	Hajela et al. (2019), Troja et al. (2020)
2019 Aug 29	741	Chandra	2.41×10^8	2.19×10^{-4}	$+0.81_{-0.65} \times 10^{-4}$	Y	Hajela et al. (2019), Troja et al. (2020)
2020 Mar 13	938	Chandra	2.41×10^8	1.30×10^{-4}	$+0.59_{-0.46} \times 10^{-4}$	Y	Hajela et al. (2020), Troja et al. (2020)
Optical (HST) measurements							
2017 Dec 4	109	HST/F160W	1.88×10^5	<0.363	...	N	Lyman et al. (2018)
2017 Dec 4	109	HST/F814W	3.80×10^5	0.109	0.017	Y	Lyman et al. (2018)
2017 Dec 4	109	HST/F140W	2.14×10^5	<0.276	...	N	Lyman et al. (2018)
2017 Dec 6	111	HST/F606W	5.06×10^5	0.111	0.019	N	Fong et al. (2019)
2018 Jan 2	137	HST/F606W	5.06×10^5	0.084	0.018	N	Fong et al. (2019)
2018 Jan 29	165	HST/F606W	5.06×10^5	0.091	0.016	N	Fong et al. (2019), Piro et al. (2019)
2018 Feb 5	170	HST/F814W	3.80×10^5	0.113	0.019	Y	Lamb et al. (2019)
2018 Feb 5	172	HST/F606W	5.06×10^5	0.085	0.017	N	Fong et al. (2019), Lamb et al. (2019)

Table 2
(Continued)

UT Date	ΔT [†] (days)	Telescope	ν (GHz)	F_ν (μ Jy)	σ_ν (μ Jy)	Reproc?	Original References
2018 Mar 14	209	HST/F606W	5.06×10^5	0.082	0.020	N	Fong et al. (2019), Piro et al. (2019)
2018 Mar 24	218	HST/F606W	5.06×10^5	0.063	0.018	N	Fong et al. (2019)
2018 Jun 10	297	HST/F606W	5.06×10^5	0.044	0.014	N	Fong et al. (2019), Lamb et al. (2019)
2018 Jul 11	328	HST/F606W	5.06×10^5	0.034	0.011	N	Fong et al. (2019), Lamb et al. (2019)
2018 Jul 20	337	HST/F606W	5.06×10^5	<0.048	...	N	Fong et al. (2019)
2018 Aug 8	355	HST/F814W	3.80×10^5	<0.058	This work (PI: Tanvir)
2018 Aug 15	362	HST/F606W	5.06×10^5	0.027	0.007	N	Fong et al. (2019), Lamb et al. (2019)
2019 Mar 24	584	HST/F606W	5.06×10^5	<0.019	...	N	Fong et al. (2019)

Notes. Correction factors of 0.6 and 0.8 have been applied to the eMERLIN and ATCA flux density values, respectively.

[†] VLITE is the VLA Low Band Ionosphere and Transient Experiment.

(This table is available in machine-readable form.)

the flux density and bandpass calibrator. The data were calibrated and flagged for radio frequency interference (RFI) using the CASA pipeline (version 5.4). We then split and imaged the target data using the CASA tasks `split` and `clean`.

For all data sets, imaging involved Briggs weighting with a robust value between 0 and 0.5, and a threshold of $3\times$ the thermal noise. For any radio image (VLA and other telescopes, described below), we measured the peak flux density of a point source (e.g., GW170817 and comparison sources) as the pixel value at the actual source position, as appropriate for point sources. The associated uncertainty is the rms noise in a source-free region of the image in the vicinity of the target. Note that the VLA absolute flux density calibration is accurate to about 5% at the L-band through to the Ku-band (Perley & Butler 2017, 1–18 GHz).

2.2. ATCA

We observed GW170817 with the ATCA (PI: Dobie, Piro) over four epochs between 2018 November to 2019 September (Table 2). We determined the flux scale and bandpass response for all epochs using the ATCA primary calibrator PKS B1934–638. Observations of PKS B1245–197 were used to calibrate the complex gains. All observations used two bands of 2048 MHz centered at 5.5 and 9.0 GHz.

We reduced the visibility data using standard MIRIAD (Sault et al. 1995) routines. The calibrated visibility data from both bands were combined, averaged to 32 MHz channels, and imported into DIFMAP (Shepherd 1997). Bright field sources were modeled separately for each band using the visibility data and a combination of point-source and Gaussian components with power-law spectra. After subtracting the modeled field sources from the visibility data, GW170817 dominates the residual image. Restored naturally weighted images for each band were generated by convolving the restoring beam and modeled components, adding the residual map and averaging to form a wideband image. Image-based Gaussian fitting with an unconstrained flux density and source position was performed in the region near GW170817. Note that the absolute flux density measurements from ATCA are accurate to about 5% (Partridge et al. 2016).

Following our Markov chain Monte Carlo (MCMC) analysis (Section 3; see also Mooley et al. 2018b) we corrected all

ATCA flux density values with a constant multiplicative factor of 0.8.

2.3. uGMRT

We reprocessed archival upgraded Giant Metrewave Radio Telescope (uGMRT) Band 5 (1.0–1.4 GHz) data with the CASA package. The data were initially flagged and calibrated using a custom developed pipeline in CASA.³⁷ The data were further inspected for RFI and flagged using standard tasks in CASA. The target source data were then imaged with the CASA task `clean`. A few rounds of phase-only self-calibration and two rounds of amplitude and phase self-calibration were done in order to approach thermal noise. The flux density of the GW source at multiple epochs is listed in Table 2.

The uGMRT Band 4 (0.55–0.85 GHz) observations were processed using the SPAM pipeline (Intema et al. 2009, 2017) by splitting the wideband data in six frequency chunks of 50 MHz wide that are processed separately. For each observing session, instrumental calibrations are derived using the best available scan on flux calibrator 3C 147 or 3C 286. These calibrations are applied to the target visibility data, after which these data are split into separate files. The target files per epoch are concatenated and taken through several cycles of self-calibration, imaging, and flagging of bad data. The final two cycles include direction-dependent calibration to mitigate ionospheric effects. The pipeline yields an image and calibrated visibility data set for each frequency chunk. In a final step, to benefit from the improved sensitivity and uv -coverage of the wideband data, the calibrated visibility data of the six frequency chunks per epoch are jointly imaged using WSClean (Offringa et al. 2014). Note that the uGMRT measurements have a systematic uncertainty of between 10% and 15% (Chandra & Kanekar 2017, in this work we assume 10% for model fits).

2.4. MeerKAT

GW170817 was observed with the MeerKAT telescope (Camilo et al. 2018; Jonas & MeerKAT Team 2018) over seven epochs between 2018 January 18 and September 2 (see Table 2). The first observation was performed during the ARI phase using 16 antennas, while remaining observations used the full 64 antenna array. All observations were centered at

³⁷ <http://www.ncra.tifr.res.in/~ishwar/pipeline.html>

1.3 GHz using 4096 channels spanning 856 MHz and an 8 s integration time. About 10% of the band was flagged due to the bandpass roll off, resulting in an effective bandwidth of 770 MHz, and a further 27% was flagged due to RFI. At 1.3 GHz, the field of view (full width at half maximum of the primary beam) is about 1° . The data were processed using the *Containerized Automated Radio Astronomy Calibration* pipeline (CARACal; Ramatsoku et al. 2020), which performs: (i) automatic RFI flagging using CASA and AOfLAGger (Offringa et al. 2010); (ii) a standard cross-calibration (delay, bandpass, and gain calibration) using a combination of CASA and MeqTrees (Noordam & Smirnov 2010), for which we used PKS 1934–638 as the primary calibrator and 3C 286 as the secondary calibrator; and (iii) a direction-dependent self-calibration (Pearson & Readhead 1984) that uses a combination of WSClean (Offringa et al. 2014), CubiCal (Kenyon et al. 2018), and PyBDSF (Mohan & Rafferty 2015). After the cross-calibration step, we found a variability of around 10% on the flux density measurements between epochs, which was corrected by bootstrapping the fluxes to a common flux scale using two reference point-like sources (see Table 1) within $2'$ of the afterglow position. It is worth noting that this uncertainty is due to our calibration process, and is not a limitation of the telescope. The self-calibration included a model of the MeerKAT primary beam that was derived from Holography measurements of the array (Asad et al. 2021).

2.5. eMERLIN

We observed GW170817 with the eMERLIN array between 2018 January and March with 11 individual runs. Each run had a duration of 5–6 hr. Observations were conducted using the C band receiver tuned at frequencies between 4.82 and 5.33 GHz, for a total bandwidth of 512 MHz distributed in four spectral windows, each one divided into 512 channels. The phase reference source was J1311–2329. Flux density calibration and bandpass correction were obtained from 3C 286 and OQ208, respectively. The observations were primarily at low elevations ($<20^\circ$), and the flux density measurements may be affected by a small bias due to the reduced gain sensitivity of the telescopes at these elevations. Nevertheless, the core of the host galaxy was detected (at $160 \pm 20 \mu\text{Jy beam}^{-1}$) in almost all runs, with an associated variability of about 12% between runs, compatible with the expected uncertainties (Garrington et al. 2004; Muxlow et al. 2020). We measured the flux density of NGC 4993 to be $0.25 \pm 0.01 \text{ mJy beam}^{-1}$ at 4.5 GHz with the VLA (Mooley et al. 2018a), indicating a flux density correction factor of about 0.6 for the eMERLIN measurements. The flux density of GW170817 (detected only in the first observing run, on 2018 January 14), the associated uncertainty, and the 3σ upper limits reported in Table 2 include the absolute flux density error (25%) and statistical map noise error.

2.6. HST

Reduced HST images were downloaded from the MAST archive. To remove most of the stellar light we first fit a simple Sérsic model to NGC 4993 using Galfit (Peng et al. 2002). This left significant residuals (asymmetries, dust lanes, shell/tidal features, etc.) that were removed by applying a $1''$ box median filter. This was followed by astrometric correction to align the images with each other. To obtain point-spread function (PSF) photometry at the expected position of GW170817 we have

done the following. (1) We estimated an empirical PSF model (50×50 pixel size) by first detecting point-like sources using SExtractor (Bertin & Arnouts 1996), and constructing an average PSF from these. Sources that did not fit well to the average PSF were removed, and a final PSF was constructed using the remaining point-like sources. (2) We fit the PSF model to the data at the expected position of GW170817. Uncertainties and limiting magnitudes were estimated by randomly (>100 times) fitting the PSF model to the background as close to the position of GW170817 as possible.³⁸

In Table 2 we report the upper limit from a previously unpublished data set. The observations (PI: N. Tanvir) were carried out with the WFC3/UVIS detector using F814W on 2018 August 08.4 and have a total exposure time of 5.2 ks.

2.7. Chandra and XMM-Newton

We list the Chandra and XMM-Newton observational data on GW170817 used here for spectral analysis in Table 3.

For Chandra we used CIAO v4.13 (Fruscione et al. 2006) with CALDB v4.9.5 to analyze the data, initially reprocessing the data using the `chandra_repro` tool. We then astrometrically aligned the events of each individual obsID to a common frame, which is important when the X-ray emission from GW170817 is not detected in an individual observation. To do this we first ran `wavdetect` on events in the 0.5–8 keV range with wavelet scales of 1, 2, and 4 pixels and all other parameters set as default to get the positions of the X-ray sources detected in each observation. This yielded ~ 200 –500 source positions depending on the exposure. We then used `wcs_match` to obtain the transform matrix, and the source list from obsID 20860 as the reference, as done in Hajela et al. (2021), filtering to sources within $1''$ of each other and a residual limit of $1''$. The typical residual was then $\sim 0''.5$. We used `wcs_update` and the resulting transform matrix to align the astrometry of each obsID to the reference frame.

The tool `specextract` was used to extract the X-ray spectra of GW170817 and its host galaxy NGC 4993. For GW170817, we used a circular region with radius $1''$, which encompasses 90% of the PSF at 1.5 keV, centered on the source. We extracted background events from a nearby source-free circular region with radius $19''.2$. We did not weight the ARFs generated by `specextract` (“weight = no”), which is appropriate for a point-like source. In an earlier version of this paper, we set “psfcorr = yes”; however, this was determined to overestimate the PSF correction,³⁹ which is likely the reason for the discrepancy in fluxes found by Troja et al. (2021). We therefore used the tool `arfcorr` as a work-around to correct the ARFs and incorporate the PSF correction.

For groups of observations made close to each other, in order to increase signal-to-noise ratios, we combined the spectral products using the CIAO tool `combine_spectra` for use in spectral fitting.

To measure the emission from NGC 4993, we extracted events from a $50''$ circular region centered on the nucleus,

³⁸ We have validated our PSF photometry method by comparing the resulting light curve of GW170817 in the F606W filter with that published by Fong et al. (2019). The methods agree within the uncertainties. For F606W we preferred to use the Fong et al. (2019) flux density values for our final panchromatic data set (Table 2) due to the more precise background subtraction (the availability of an observation template for the subtraction of the host galaxy, as done by Fong et al. (2019)). Nevertheless, the precision of the flux density measurements is comparable for both methods ($\sim 20\%$).

³⁹ <https://cxc.harvard.edu/ciao/ahelp/specextract.html>

Table 3
Chandra and XMM-Newton Observational Data

ObsID	Exposure (ks)	Start Date (UT)	PI	Count Rate (ks ⁻¹)	Flux (10 ⁻¹⁴ erg cm ⁻² s ⁻¹)
Chandra observations					
18955	24.64	2017 Aug 19	Fong	<0.12	<0.27
19294	49.41	2017 Aug 26	Troja	0.24 ± 0.07	0.52 ^{+0.29} _{-0.21}
20728	46.69	2017 Sep 1	Troja	0.34 ± 0.09	0.66 ^{+0.31} _{-0.24}
18988	46.69	2017 Sep 2	Haggard	0.25 ± 0.07	0.51 ^{+0.29} _{-0.21}
20860	74.09	2017 Dec 3	Wilkes	1.34 ± 0.13	2.55 ^{+0.44} _{-0.40}
20861	24.74	2017 Dec 6	Wilkes	1.25 ± 0.22	2.44 ^{+0.80} _{-0.65}
20936	31.75	2018 Jan 17	Wilkes	1.63 ± 0.23	3.46 ^{+0.85} _{-0.73}
20938	15.86	2018 Jan 21	Wilkes	1.70 ± 0.33	3.23 ^{+1.14} _{-0.92}
20937	20.77	2018 Jan 23	Wilkes	1.30 ± 0.25	2.63 ^{+0.92} _{-0.75}
20939	22.25	2018 Jan 24	Wilkes	0.94 ± 0.21	1.91 ^{+0.77} _{-0.61}
20945	14.22	2018 Jan 28	Wilkes	0.84 ± 0.24	2.01 ^{+1.12} _{-0.81}
21080	50.79	2018 May 3	Wilkes	0.65 ± 0.11	1.27 ^{+0.40} _{-0.33}
21090	46	2018 May 5	Wilkes	0.75 ± 0.13	1.43 ^{+0.44} _{-0.37}
21371	67.17	2018 Aug 10	Troja	0.41 ± 0.08	0.83 ^{+0.29} _{-0.24}
21322	35.64	2019 Mar 21	Margutti	0.14 ± 0.06	0.43 ^{+0.41} _{-0.25}
22157	38.19	2019 Mar 22	Margutti	0.15 ± 0.06	0.31 ^{+0.27} _{-0.17}
22158	24.93	2019 Mar 23	Margutti	0.08 ± 0.06	0.31 ^{+0.54} _{-0.25}
21372	40	2019 Aug 27	Troja	0.02 ± 0.03	0.06 ^{+0.08} _{-0.08}
22736	33.61	2019 Aug 29	Troja	0.09 ± 0.05	0.27 ^{+0.35} _{-0.19}
22737	25.25	2019 Aug 30	Troja	0.16 ± 0.08	0.88 ^{+0.95} _{-0.55}
21323	24.29	2020 Mar 9	Margutti	0.08 ± 0.06	0.34 ^{+0.58} _{-0.27}
23183	16.28	2020 Mar 13	Margutti	<0.18	<0.57
23184	19.85	2020 Mar 15	Margutti	0.10 ± 0.07	0.64 ^{+1.08} _{-0.50}
23185	36.18	2020 Mar 15	Margutti	0.02 ± 0.03	0.07 ^{+0.09} _{-0.09}
XMM-Newton observations					
811210101	26.36	2017 Dec 29	Schartel	2.17 ± 0.40	2.56 ^{+0.85} _{-0.78}
811212701	48.12	2018 Jan 26	Schartel	1.82 ± 0.27	2.03 ^{+0.57} _{-0.52}

Note. Count rates are observed (not corrected for PSF losses) in the 0.5–8 keV band for Chandra and 0.2–10 keV band for XMM-Newton. Fluxes are in the 0.3–10 keV band and are corrected for Galactic absorption.

masking six point sources lying within the region (including GW170817 and the active galactic nucleus (AGN) associated with the galaxy). We used a circular source-free region, with radius 34", outside the galaxy extraction region, to estimate the background. For the emission from the galaxy, since we do not expect this to change significantly over time, we combined spectral products from all Chandra observations.

We used XMM-SAS v18.0.0 to analyze the XMM-Newton data and the tool `evselect` to extract spectral and light-curve data. We did not use XMM-Newton obsID 0830191001 since the source was too faint with respect to the AGN for spectral analysis. Count rates greater than 0.7 s⁻¹ in the range 10–12 keV on the pn detector were used to determine periods of high background data, which were excluded from our analysis. Significant background flaring resulted in only 26 and 48 ks filtered exposures for obsIDs 0811210101 and 0811212701, respectively. Source events were then extracted from a circular region with radius 5" centered on GW170817. While this is less than 50% of the EPIC-pn encircled energy, it was necessary to use a small region in order to exclude emission from the AGN, which is only 10" from the source. In order to account for the AGN, we extracted background events from a region at the same distance from the AGN as GW170817.

For both GW170817 and NGC 4993, the spectra were grouped with a minimum of 1 count per bin with the HEASOFT tool `grppha`. We used the X-ray spectral fitting package XSPEC v12.10.1 to fit the data. For GW170817 we fit the data with an absorbed power-law model (`tbabs*ztbabs*powerlaw`), where `tbabs` is a neutral absorbing column attributed to our own Galaxy, fixed at 7.59×10^{20} cm⁻² (HI4PI Collaboration 2016—HI4PI Map), and `ztbabs` is a neutral absorbing column intrinsic to the source, $N_{\text{H,NGC 4993}}$, at $z = 9.73 \times 10^{-3}$, which we initially allowed to vary within the fit. We used the Cash statistic as the fit statistic, with the background subtracted, and the spectra were fit in the 0.5–8 keV range for Chandra and the 0.2–10 keV range for XMM-Newton.

We initially allowed all spectral parameters to vary across observational epochs to test for spectral variations, however we did not find any evidence for this. We therefore re-fit the spectra with the $N_{\text{H,NGC 4993}}$ and Γ parameters tied across all epochs. We found no evidence for absorption intrinsic to the source with a 90% upper limit of $N_{\text{H,NGC 4993}} < 5 \times 10^{20}$ cm⁻². For the power law, the best-fit photon index is $\Gamma = 1.62^{+0.13}_{-0.09}$ (1 σ errors), which is consistent with $\Gamma = 1.584$ that is inferred from the radio to X-ray spectrum (confirmed in Section 3).

Table 4
Parameters Estimated from Modeling the Afterglow Light Curve

Parameter	Value	Units
Broken Power-law/Analytical Jet Model		
$F_{\nu,p}$	101 ± 3	μJy
t_p	155 ± 4	days
α_1	0.86 ± 0.04	
α_2	$-1.92^{+0.10}_{-0.12}$	
$\log_{10}(s)$	$0.56^{+0.12}_{-0.11}$	
β	-0.584 ± 0.002	
χ^2/dof	75/97	
p	2.168 ± 0.004	
E/m_{ISM}	$\simeq 1.5 \times 10^{53}$	erg cm^3
θ_v	$\simeq 14\text{--}20$	degrees
θ_j	$\simeq 1\text{--}4$	degrees
Structured jet model		
θ_v	35.2 ± 0.6	degrees
ϵ_e	$7.8^{+1.0}_{-0.6} \times 10^{-3}$	
ϵ_b	$9.9^{+4.7}_{-2.2} \times 10^{-4}$	
p	$2.07^{+0.01}_{-0.02}$	
n_{ISM}	$9.8^{+0.2}_{-1.6} \times 10^{-3}$	cm^{-3}
χ^2/dof	95.2/97	

Therefore we fixed⁴⁰ $N_{\text{H,NGC 4993}}$ (intrinsic) = 0 and $\Gamma = 1.584$ in order to measure the flux from GW170817. We calculated the 0.3–10 keV flux and its uncertainty, corrected for the absorption from our own Galaxy, using the model `cflux` in XSPEC, which is presented in Table 3 along with the observed count rates (i.e., not corrected for PSF losses).

The flux density was determined from the normalization of the power law, which is a measure of the flux density at 1 keV in μJy when the commands “`xset pow_emin 1.0`” and “`xset pow_emax 1.0`” are used in XSPEC. We used the “`error`” command in XSPEC to determine the uncertainties, with a delta-C-stat of 1.0, which corresponds to a 1σ confidence level for one free parameter.

The X-ray emission from GW170817 was detected by Chandra in all but four observations, obsIDs 18955, 23183, 24923, and 24924. We calculated the 3σ upper limit on the count rate of GW170817 in these observations from events extracted in the background region. We determined that the background count rate in the source extraction region is $(6\text{--}8) \times 10^{-6}$ counts s^{-1} . By using the Poisson probability distribution, the 3σ upper limit on the source count rate was calculated to be $(1\text{--}2) \times 10^{-4}$ counts s^{-1} , which when assuming our spectral model corresponds to a 0.3–10 keV unabsorbed flux of $(3\text{--}6) \times 10^{-15}$ erg cm^{-2} s^{-1} . We present the individual upper limits on the count rates and fluxes in Table 3. As noted in Troja et al. (2021), these upper limits are systematically lower than they calculated due to the differing statistical treatment, as they used a Bayesian method and we used classical Poisson statistics.

⁴⁰ We believe that $\Gamma = 1.584$ is robust, but to understand the effect of changing Γ we did a test. We recalculated the X-ray flux density values by changing Γ by 0.2 (i.e., we used $\Gamma = 1.38$ and $\Gamma = 1.78$) and then redid the MCMC fitting of the full afterglow light curve as described in Section 3. We found that the value of spectral index β (reported in Table 4) changed by $<1.5\sigma$ and the change in the other fit parameters was negligible, $\ll 1\sigma$. We also repeated the MCMC analysis by leaving $\Gamma (= 1 - \beta)$ as a free parameter and found the best-fit value of beta to be similar (-0.583 ± 0.003).

Overall, we detected 9604 counts between 0.5 and 8 keV in the source extraction region from all observations combined, of which 9.4% are attributable to NGC 4993. We used a power-law model to calculate a flux, where the power-law index $\Gamma = 0.7 \pm 0.6$, and the normalization $N = 1.8 \pm 1.0 \times 10^{-6}$, yielding a 0.5–8 keV flux of $2.0^{+1.1}_{-0.7} \times 10^{-14}$ erg cm^{-2} s^{-1} . Since the source counts are a small fraction of the total (source + background) counts, background subtraction introduces large uncertainties into the spectral modeling results, which should be treated with caution.

We also point the reader to Hajela et al. (2019, 2020), who did a similar and independent analysis using the Chandra data. Additionally, we note that the X-ray data have been processed independently also by Troja et al. (2017, 2018, 2019), Piro et al. (2019), and Troja et al. (2020, 2021).

3. Analytical Modeling

Following previous afterglow studies (Alexander et al. 2018; Dobie et al. 2018; Mooley et al. 2018b), we fit the afterglow data⁴¹ using a smoothly broken power-law model,

$$F(t, \nu) = 2^{1/s} \left(\frac{\nu}{3 \text{ GHz}} \right)^\beta F_p \times \left[\left(\frac{t}{t_p} \right)^{-s\alpha_1} + \left(\frac{t}{t_p} \right)^{-s\alpha_2} \right]^{-1/s} \quad (1)$$

where ν is the observing frequency, β is the spectral index, F_p is the flux density at 3 GHz at light-curve peak, t is the time post-merger, t_p is the light-curve peak time, s is the smoothness parameter, and α_1 and α_2 are the power-law rise and decay slopes, respectively. This MCMC fitting was done⁴² using the Python package `emcee` (Foreman-Mackey et al. 2013). We obtained best-fit values listed in Table 4. Figure 2 shows the best-fit broken power-law curve and the resulting residuals. Figure 3 shows the corner plot corresponding to the MCMC analysis.

We used a rough analytic model, described in Mooley et al. (2018b), to estimate the jet opening angle θ_j and the viewing angle θ_v . The sharpness of the light-curve peak, $\Delta t/t = (t_2 - t_1)/t_2$, where t_1 is the time around the transition from the $t^{0.86}$ rise to the peak and t_2 is the time when the light curve approaches t^{-2} , is directly related to the ratio θ_j/θ_v . Using the approximations $\theta_v - \theta_j \gg \theta_j$ and jet Lorentz factor $\Gamma \propto t^{-3/8}$ (Blandford & McKee 1976) we found that $\Delta t/t \simeq (8/3)\theta_j/\theta_v$. Here, we used the approximation that θ_j/θ_v is much smaller than unity. From our MCMC analysis we found $0.2 \lesssim \Delta t/t \lesssim 0.4$ (68% confidence or better, depending on where t_1 and t_2 lie), indicating that $0.1\theta_v \lesssim \theta_j \lesssim 0.2\theta_v$. Using

⁴¹ We did not consider the gVLBA and eMERLIN data points while modeling since they have relatively large uncertainties in the absolute flux calibration.

⁴² We chose 100 walkers, 1000 steps, and flat priors on all of the parameters. Since compact interferometric data may be affected by extended emission from the host galaxy, we also introduced a scale factor into the MCMC fit to explore possible offsets in the ATCA, MeerKAT, and uGMRT flux densities. We recovered the constant flux multiplication factor of 0.8 for the ATCA (most likely due to the compact array being sensitive to extended structure around GW170817; Mooley et al. 2018b), while the factor is consistent with unity for the MeerKAT and uGMRT data. The inclusion of scale factors in the MCMC fitting gave best-fit values and uncertainties of all other parameters in the fit to be almost the same as those reported in Table 4, except for parameters F_p , t_p , and $\log_{10}(s)$ where the uncertainties were larger by factors of ~ 2 than the ones given in Table 4.

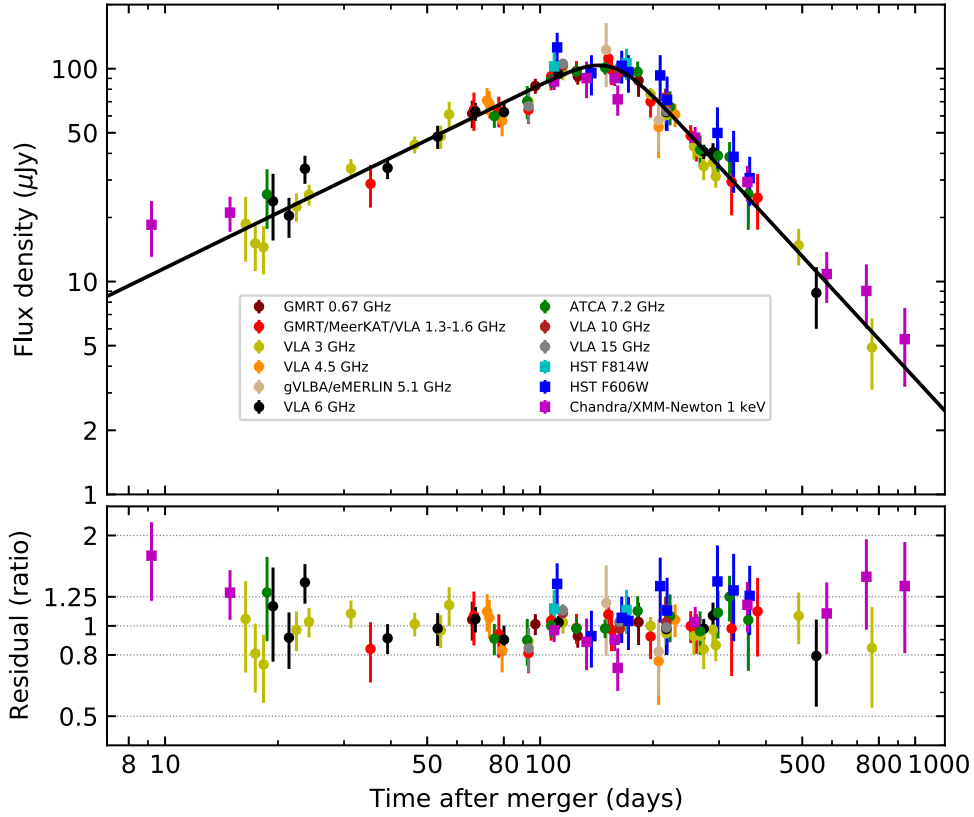


Figure 2. Broken power-law fit (using MCMC; the best fit is shown as a black curve in the upper panel and residuals are shown in the lower panel) to the afterglow light curve. The corner plot for the MCMC analysis is shown in Figure 3. The light curve is scaled to 3 GHz using the best-fit spectral index (-0.584) derived from the MCMC analysis. Color coding is the same as in Figure 1. The light curve rises as $t^{0.86 \pm 0.04}$ and declines as $t^{-1.92 \pm 0.12}$. The light-curve peak occurs at 155 ± 4 days post-merger. The lack of any substantial outlier data points indicates that the afterglow is optically thin throughout its evolution, with the synchrotron self-absorption frequency lying below the radio band and cooling frequency lying above the soft X-ray band. See Section 3 for details.

$\Gamma \simeq 4.1 \pm 0.5 \simeq 1/(\theta_v - \theta_j)$ close to the peak of the light curve from the VLBI measurement (Mooley et al. 2018a), we got $\theta_j \simeq 1^\circ - 4^\circ$ and $\theta_v \simeq 14^\circ - 20^\circ$.

Using the Blandford–McKee solution (Blandford & McKee 1976), we can estimate the ratio of the jet kinetic energy and the density of the circum-merger environment E/n_{ISM} . We have

$$E/n_{\text{ISM}} \simeq \theta_j^2 R^3 \Gamma^2 m_p c^2 \simeq 8 \theta_j^2 t^3 \Gamma^8 m_p c^5 \quad (2)$$

since $R = \beta c t_{\text{lab}} = (1 - 1/2\Gamma^2)c(1 - \beta \cos(\theta_v))^{-1}t \simeq 2\Gamma^2 ct$, where R is the distance traveled (in the lab frame) by the blast wave, t_{lab} is time in the lab frame, m_p is the proton mass, and c is the speed of light. Hence, $E/n_{\text{ISM}} \simeq 1.5 \times 10^{53} (\theta_j/3^\circ)^2 \text{ erg cm}^3$.

4. Constraints on the Merger Environment and Merger Remnant

4.1. ISM Density Estimate Using the Diffuse X-Ray Emission from NGC 4993

In Section 2.7 we described the X-ray data analysis, including the diffuse X-ray emission from NGC 4993, where we calculated a flux of $2.0_{-0.7}^{+1.1} \times 10^{-14} \text{ erg cm}^{-2} \text{ s}^{-1}$, which corresponds to a luminosity of $L_{0.5-8} \sim 2 \times 10^{39} \text{ erg s}^{-1}$.

Because of the large uncertainty due to the background subtraction, we cannot separate the diffuse emission of the hot ionized ISM from that arising from unresolved point sources based on their spectral shapes. Therefore, we used the 2σ upper

limit on the X-ray flux to estimate an limit on the number density of the hot ionized ISM in NGC 4993. To obtain the density at the location of the merger from the diffuse emission in the circular region with radius $34''$, we used an isothermal beta model (Cavaliere & Fusco-Femiano 1978) to describe the global structure of the hot ionized gas. This model is characterized by the density at the galactic center, the core radius, r_c , the power-law index of the density profile, β_{ISO} , and temperature T . For early-type galaxies with a diffuse X-ray luminosity of $\lesssim 10^{40} \text{ erg s}^{-1}$, the model parameters are typically in the range of $0.1 \lesssim T \lesssim 1 \text{ keV}$, $r_c \lesssim 10 \text{ kpc}$, and $0.25 \lesssim \beta_{\text{ISO}} \lesssim 1$ (Babyk et al. 2018). Given the density structure and the X-ray emissivity calculated with APEC, we computed the total X-ray flux arising from the hot ionized ISM in the circular region. Assuming $\beta_{\text{ISO}} = 0.5$ and the solar metallicity, we obtained a 2σ upper limit on the ISM density at the merger, $\lesssim 10^{-2} \text{ cm}^{-3}$, as shown in Figure 4. Note that our method provides a good estimate of the mean density of the hot ionized ISM, but it does not necessarily provide a precise estimate of the density at the merger location. However, our estimate is consistent with the result of Hajela et al. (2019)— $n \leq 9.6 \times 10^{-3} \text{ cm}^{-3}$ —in which they analyzed the X-ray data in a small annular region of the inner part of NGC 4993. The consistency of these two independent analyses supports $n \lesssim 10^{-2} \text{ cm}^{-3}$. Furthermore, this estimate is consistent with that estimated from the afterglow light curve and superluminal motion modelings (e.g., Mooley et al. 2018a) and from searches for neutral gas ($n < 0.04 \text{ cm}^{-3}$; Hallinan et al. 2017).

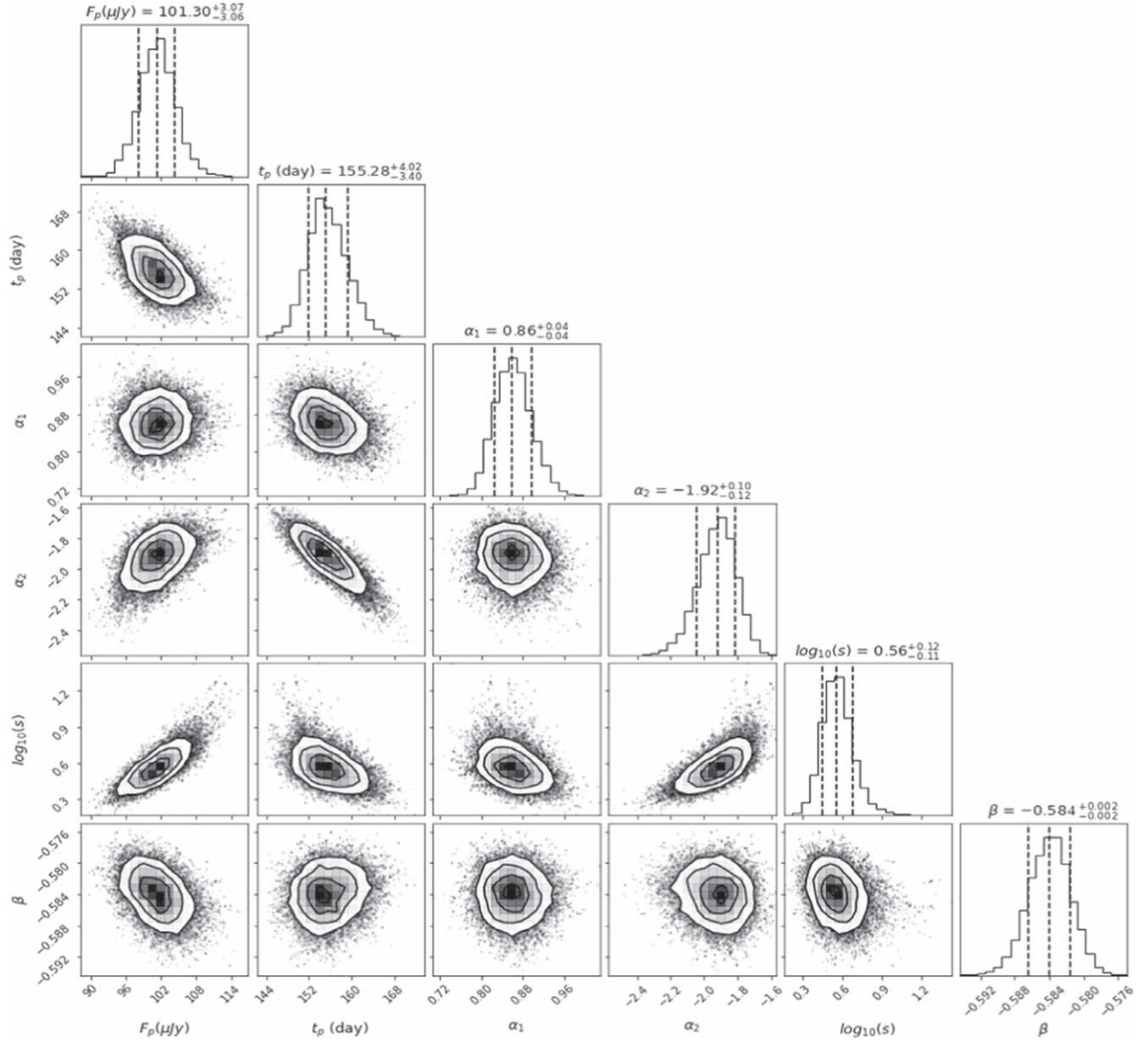


Figure 3. Corner plot for broken power-law fit to the light curve presented in Figure 2. Here, β is the spectral index, F_p is the flux density at 3 GHz at light-curve peak, t_p is the light-curve peak time, and α_1 and α_2 are the power-law rise and decay slopes, respectively.

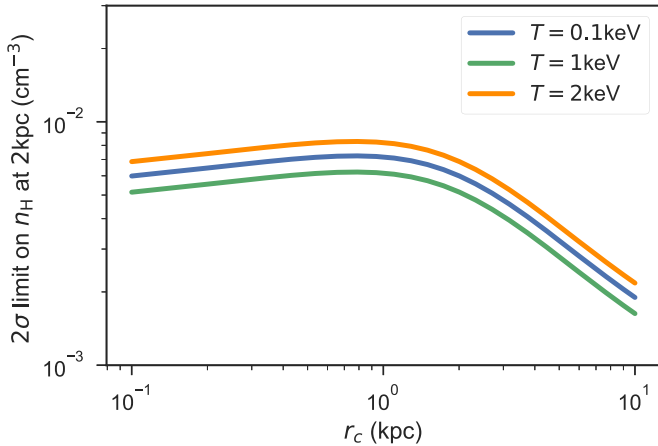


Figure 4. Upper limits on the number density of the hot ionized ISM at the merger location (~ 2 kpc from the center of NGC 4993) as a function of the core radius (r_c) at the temperature (T) of the hot ISM. Here, we assume the solar metallicity and $\beta_{\text{ISO}} = 0.5$.

4.2. The Merger Remnant

While GW170817 is believed to have collapsed to a black hole after a short-lived hypermassive neutron star phase, the exact nature of the remnant remains observationally unknown (e.g., Kasen et al. 2017; Pooley et al. 2018; Yu et al. 2018). Here, we derive constraints on the magnetic field strength (B) of any long-lived neutron star remnant⁴³ that may have resulted from GW170817. The afterglow flux density measurements up to 940 days post-merger indicate that the late-time afterglow is consistent with a decelerating jet (t^{-p} decline). The full uniform afterglow light curve is shown in Figure 1. We consider an upper limit (measured flux density + 2σ uncertainty) of 3.6×10^{-10} Jy on the X-ray flux density, corresponding to a luminosity of 2×10^{38} erg s $^{-1}$ for any pulsar wind component. Pulsar (magnetic dipole) spin-down

⁴³ Here, we do not consider any energy loss from gravitational wave radiation. For an alternative analysis that considers such radiation, see Piro et al. (2019).

luminosity is given by (Spitkovsky 2006; Hotokezaka et al. 2017; Metzger 2017)

$$L_{\text{sd}} \simeq 2.3 \times 10^{43} \text{ erg s}^{-1} \left(\frac{B}{10^{12} \text{ G}} \right)^2 \times \left(\frac{P}{1 \text{ ms}} \right)^{-4} \left(1 + \frac{t}{t_{\text{sd}}} \right)^{-2} \quad (3)$$

where,

$$t_{\text{sd}} \simeq 31 \text{ yr} \left(\frac{B}{10^{12} \text{ G}} \right)^{-2} \left(\frac{P}{1 \text{ ms}} \right)^2. \quad (4)$$

Assuming the spin period at the time of merger is $P \simeq 1$ ms and that a fraction $f \simeq 10^{-2}$ of the spin-down power is converted into X-ray radiation, we obtained⁴⁴ $B \lesssim 10^{10.4}$ G.

The sensitive late-time afterglow measurement is therefore more constraining than the previous constraints (Margutti et al. 2018; Pooley et al. 2018) on the magnetic field strength. The upper limit of $10^{10.4}$ G is at odds with simulations⁴⁵ (Zrake & MacFadyen 2013; Kiuchi et al. 2014; Giacomazzo et al. 2015) that predict $B \sim 10^{15}$ – 10^{16} G. If the simulations accurately represent the dipole magnetic field strength, then it is likely that the merger remnant in GW170817 is a black hole.

However, we note that we are not able to rule out magnetars with $B \gtrsim 10^{16}$ G since for such objects the spin-down luminosity would decrease rapidly within the first ~ 100 days (this is a very conservative timescale over which the merger ejecta would become optically thin toward any emission arising from spin-down), below the afterglow luminosity measured for GW170817 (see Figure 7 of Margutti et al. 2018, for example).

5. Numerical Modeling

We have presented the uniform afterglow light curve to the astronomical community with the hope that these data will be used for extensive modeling in the future. In this section we provide a preliminary⁴⁶ update on the jet and ISM parameters obtained using the numerical model from Lazzati et al. (2018; Section 5.1). In Section 5.2 we review and contrast with previous modeling efforts.

5.1. Structured Jet Model

We modeled the data with a forward-shock afterglow model based on the semi-analytic code used in Lazzati et al. (2018). The model has five free parameters: the viewing angle θ_v , the microphysical parameters ϵ_e (the fraction of shock energy given to electrons) and ϵ_B (the fraction of shock energy given to tangled magnetic field), the electrons population distribution index p , and the external medium density n_{ISM} , which was assumed to be constant. The total kinetic energy of the fireball and its initial Lorentz factor, both dependent on the viewing angle, were taken from a hydrodynamic numerical simulation previously described in Lazzati et al. (2017). Specifically, the energy of the blast wave, set by the numerical simulation, is 6×10^{49} erg. The fit was performed with a dedicated implementation of an MCMC scheme, assuming flat priors

⁴⁴ This lower limit on the magnetic field strength is sensitive to f and P . If $f = 10^{-3}$ or $P = 2$ ms then we get $B \lesssim 10^{11}$ G.

⁴⁵ We assume here that the small-scale magnetic fields, found in simulations, are comparable in strength to the global dipolar field.

⁴⁶ The model currently excludes VLBI constraints and assumes a constant jet opening angle and blast-wave energy.

for all free parameters except the ISM density, which was assumed to be small ($n_{\text{ISM}} \leq 0.01 \text{ cm}^{-3}$; see Section 4 and Hallinan et al. 2017). The best-fit parameters are given in Table 4. The fit to the light curve and corresponding corner plot are shown in Figure 5.

We caution that the quoted uncertainties in the best-fit results are purely statistical and do not reflect the potentially large systematic uncertainties associated with the numerical simulation itself. We have modeled the jet dynamics and merger ejecta interaction as a purely hydrodynamical system using FLASH (Fryxell et al. 2000), which does not have magneto-hydrodynamic capabilities for relativistic flows. This can affect the final polar distribution of both the kinetic energy of the merger and the Lorentz factor of the outflow. Additionally, the FLASH simulation uses a set of initial conditions that do not necessarily reproduce the actual conditions at the base of the jet (Lazzati et al. 2017). Finally, it should be noted that the constraint on the proper motion of the radio transient (Mooley et al. 2018a) is not included in the fit.⁴⁷

5.2. Review of and Comparison with Previous Models

It is now widely accepted that GW170817 produced a relativistic jet with substantial angular structure. Multiple studies, using different hydrodynamic and semi-analytic models, have modeled the afterglow of GW170817 to obtain the properties of the structured jet. The parameter constraints derived by these studies are tabulated in Table 5. Generally, all studies obtain small jet opening angles, $\lesssim 6^\circ$, and viewing angles between 15° and 35° . Very few studies (Mooley et al. 2018a; Ghirlanda et al. 2019; Hotokezaka et al. 2019) fit the VLBI proper-motion constraint. Estimates for the isotropic equivalent energy and circum-merger density range from $10^{51.5}$ – 10^{53} erg and $10^{-1.5}$ – $10^{-4.5} \text{ cm}^{-3}$, respectively. The circum-merger density is correlated with ϵ_B , which is estimated to be between $10^{-1.5}$ and 10^{-5} . The parameters we obtain using the structure jet model are generally in agreement with the literature, although our estimate of $\theta_v = 35.2 \pm 0.6$ is the largest to date.

Resmi et al. (2018), Hotokezaka et al. (2019), Troja et al. (2019), Ghirlanda et al. (2019), Lamb et al. (2019), and Ryan et al. (2020) used semi-analytical techniques, using power-law and/or Gaussian angular profiles for the jet. Lamb et al. (2019) also used a two-component model that includes a top-hat jet and Gaussian cocoon. Only Hotokezaka et al. (2019) and Ghirlanda et al. (2019) included VLBI constraints (but these studies also neglected sideways/lateral expansion of the jet). This may be the reason why they obtained low viewing angles, $\sim 16^\circ$. The other semi-analytical studies obtained median viewing angle estimates of between 20° and 27° .

Wu & MacFadyen (2019) and Hajela et al. (2019) fit a “boosted fireball” model, a family of models parameterized by two parameters, the internal energy and boost Lorentz factor (which also define the angular structure of the structured jet), to the afterglow light curve. This technique uses a template bank constructed from 3D hydrodynamical simulations together with analytic scaling relations. Lazzati et al. (2018) used input data (jet energy and opening angle, chosen to mimic a typical SGRB) from a 3D/2D hydrodynamical simulation. Sideways expansion was neglected. This work also utilized the Lazzati et al. (2018)

⁴⁷ Our code is currently being updated to take the proper-motion constraint into account.

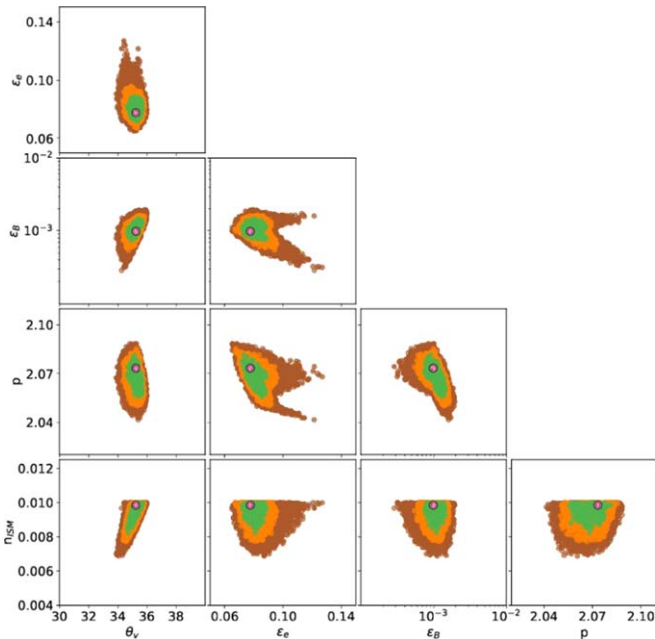
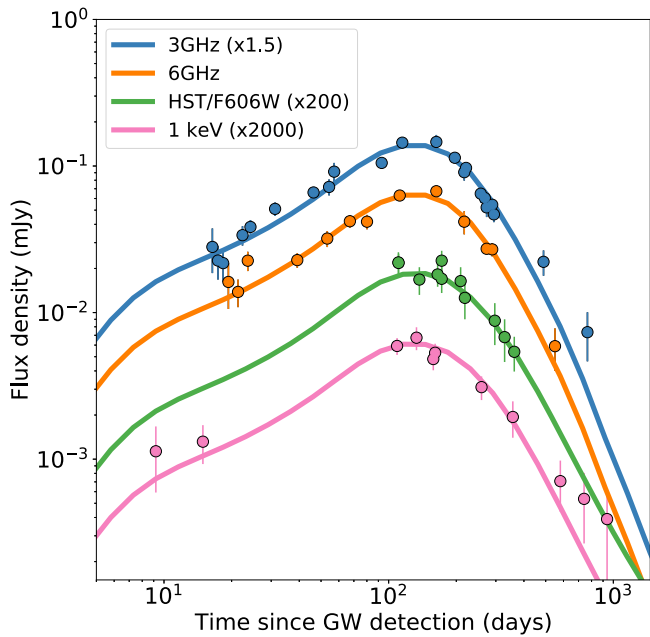


Figure 5. Upper panel: structured jet model fit to the afterglow light curve using the forward-shock model from Lazzati et al. (2018). The best-fit model from the MCMC analysis is shown and color coding is according to the observing frequency. Only a subset of the observational data is plotted in this figure. Lower panel: corner plot for the structured jet model. The pink dot shows the best-fit value for each parameter, and green indicates the 67% confidence interval. See Section 5.1 for details.

scheme. All of these studies obtained median viewing angles of larger than 30° . Mooley et al. (2018a) carried out a dozen hydrodynamical simulations using various setups to determine the parameters that can fit the afterglow light-curve and proper-motion data. They obtained a median viewing angle of about 20° , which is much smaller than that obtained by Lazzati et al. (2018), Wu & MacFadyen (2019), and Hajela et al. (2019), likely due to the VLBI proper motion being taken into account.

Looking at the substantial differences in all of these modeling results, we therefore highlight that a combined analysis of the

VLBI proper motion measured by Mooley et al. (2018a) and of the full uniform light curve presented here is crucial for obtaining an accurate estimate of the viewing angle and other parameters (jet and ISM) of GW170817.

6. Summary and Discussion

By compiling and reprocessing archival data at radio, optical, and X-ray wavelengths, and reporting new radio data, we have presented a fairly uniform data set of the afterglow of GW170817 between 0.5 and 940 days post-merger. These afterglow measurements are available in ASCII format (continuously updated as new data get published) on the web.⁴⁸ The afterglow light curve (Figure 1) shows a power-law rise, $F_\nu \propto t^{0.86}$, and a power-law decline, $F_\nu \propto t^{-1.92}$, consistent with expectations for a laterally expanding relativistic jet core (dominating the late-time afterglow emission) surrounded by low-Lorentz factor material (dominating the early-time afterglow emission). A more detailed investigation of the shape of the afterglow light curve may provide important insights into the angular structure of the relativistic outflow from GW170817, and possibly the properties of the ejecta and jet at the time of jet launch.

Our uniform panchromatic data set of the afterglow implies a spectral index of $\beta = -0.584 \pm 0.002$, leading to an extremely precise estimate of the electron power-law index, $p = 2.168 \pm 0.004$. The single unchanging spectral index across all epochs implies that the synchrotron self-absorption frequency is below the radio band and the cooling frequency is above the soft X-ray band throughout the evolution of the afterglow. The rate of decline of the afterglow light curve appears to be consistent with t^{-p} (within 2σ), indicating that sound-speed expansion may provide a sufficiently accurate description of the jet lateral expansion. We do not find any evidence for steepening beyond t^{-p} post-peak, as found by some hydrodynamical simulations (e.g., van Eerten & MacFadyen 2013).

Likewise, we do not find any evidence for flattening of the light curve during the decline phase. Specifically, we do not see any component declining as t^{-1} , even during the most recent radio observing epoch (767 days post-merger), which may be expected for a cocoon. Interpolating a t^{-1} power law backwards in time from our 3 GHz detection 767 days post-merger, we find that any cocoon contribution to the afterglow is negligible beyond ~ 90 days post-merger, i.e., the jet core has likely dominated the afterglow beyond 90 days post-merger. Even at 900 days post-merger, the lack of any flattening in the light curve indicates that the jet is still in the relativistic phase, $\Gamma\beta \gtrsim 1$. This also implies that the counter-jet and the late-time dynamical ejecta afterglow have not made their appearance yet.

In our reprocessing of the X-ray data, we do not find any evidence for significant flaring or synchrotron cooling, which argues against the presence of any long-lived magnetized neutron star remnant in GW170817 (see also Lyman et al. 2018; Hajela et al. 2019; Piro et al. 2019). By analyzing the Chandra data we also study the diffuse X-ray emission of NGC 4993. The X-ray luminosity in 0.5–8 keV is estimated to be about 2×10^{39} erg s $^{-1}$, somewhat lower than the X-ray luminosity of early-type galaxies (Babyk et al. 2018) given the total mass of NGC 4993 of $\sim 10^{12} M_\odot$ (Pan et al. 2017). We estimate the hot ionized ISM density from the observed X-ray

⁴⁸ <https://github.com/kmooley/GW170817/> or <http://www.tauceti.caltech.edu/kunal/GW170817/>.

Table 5
Summary of Published Nonthermal Afterglow Modeling for GW170817

References	Model	θ_v (deg)	θ_j (deg)	$\log_{10} E_{0.52}$ (erg)	$\log_{10} n_0$ (cm^{-3})	$\log_{10} \epsilon_e$	$\log_{10} \epsilon_B$	VLBI Fit?
This work	SJ	$35.2_{-0.6}^{+0.6}$...	-0.2	$-2.0_{-0.1}^{+0.1}$	$-1.1_{-0.1}^{+0.1}$	$-3.0_{-0.2}^{+0.1}$	N
Lazzati et al. (2018)	SJ	$33.0_{-2.5}^{+4.0}$	$-2.4_{-2.8}^{+2.1}$	$-1.2_{-1.0}^{+1.0}$	$-2.5_{-0.7}^{+0.7}$	N
Hajela et al. (2019)	BF	$30.4_{-3.4}^{+4.0}$	$5.9_{-0.7}^{+1.0}$	$-1.3_{-1.0}^{+0.0}$	$-2.6_{-0.6}^{+0.4}$	$-0.8_{-0.6}^{+0.4}$	$-2.6_{-1.2}^{+0.9}$	N
Wu & MacFadyen (2019)	BF	$30.3_{-0.4}^{+0.7}$	$6.3_{-1.7}^{+1.1}$	$-0.8_{-1.4}^{+0.2}$	$-2.0_{-1.0}^{+0.7}$	$-1.0_{-0.9}^{+0.6}$	$-3.6_{-1.3}^{+1.3}$	N
Resmi et al. (2018)	GJ	$26.9_{-4.6}^{+8.6}$	$6.9_{-1.7}^{+2.3}$	$-0.2_{-0.5}^{+0.4}$	$-2.7_{-1.0}^{+0.9}$	$-0.6_{-0.5}^{+0.1}$	$-4.4_{-0.5}^{+1.1}$	N
Ryan et al. (2020)	PLJ	$25.2_{-6.9}^{+6.9}$	$2.6_{-0.7}^{+0.7}$	$0.9_{-0.8}^{+1.1}$	$-2.6_{-1.1}^{+1.1}$	$-1.2_{-1.2}^{+0.7}$	$-3.8_{-0.9}^{+1.1}$	N
	GJ	$22.9_{-6.3}^{+6.3}$	$3.8_{-1.0}^{+1.0}$	$1.0_{-0.7}^{+1.0}$	$-2.7_{-1.0}^{+1.0}$	$-1.4_{-0.7}^{+0.7}$	$-4.0_{-0.7}^{+1.1}$	N
Troja et al. (2019)	GJ	$21.8_{-6.3}^{+6.3}$	$3.4_{-0.6}^{+1.0}$	$0.8_{-0.6}^{+0.9}$	$-2.5_{-1.0}^{+0.9}$	$-1.4_{-0.6}^{+0.5}$	$-4.0_{-0.7}^{+1.0}$	N
Lamb et al. (2019)	2C	$20.6_{-1.7}^{+1.7}$	$4.0_{-0.6}^{+0.6}$	$0.0_{-0.6}^{+0.9}$	$-3.3_{-1.6}^{+0.6}$	$-1.3_{-0.7}^{+0.6}$	$-2.4_{-0.9}^{+1.4}$	N
	GJ	$19.5_{-1.1}^{+1.1}$	$5.2_{-0.6}^{+0.6}$	$0.4_{-0.4}^{+0.5}$	$-4.1_{-0.5}^{+0.5}$	$-1.4_{-0.6}^{+0.5}$	$-2.1_{-1.0}^{+0.8}$	N
Hotokezaka et al. (2019)	GJ	$16.6_{-0.6}^{+0.6}$	$3.4_{-0.6}^{+0.6}$	Y
	PLJ	$16.6_{-0.6}^{+0.6}$	$2.9_{-0.6}^{+0.6}$	Y
Ghirlanda et al. (2019)	PLJ	$15.0_{-1.0}^{+1.5}$	$3.4_{-1.0}^{+1.0}$	$0.4_{-7.0}^{+0.6}$	$-3.6_{-0.7}^{+0.7}$...	$-3.9_{-1.6}^{+1.6}$	Y
Mooley et al. (2018a)	HD	[14, 28]	<5	[0, 1.5]	[-4, -2.3]	0.1	[-2, -5]	Y

Note. GJ = Gaussian Jet, PLJ = Power-law jet, SJ = Other structured jets, BF = Boosted fireball, HD = Hydrodynamic simulations, 2C = Two component.

flux to be $\lesssim 0.01 \text{ cm}^{-3}$. This result is consistent with that obtained from an independent analysis done by Hajela et al. (2019), as well as that estimated from the afterglow modelings of GW170817. Comparing the late-time X-ray luminosity with the pulsar spin-down luminosity, we rule out the phase space of $10^{10.4} \sim 10^{16} \text{ G}$ for the magnetic field strength of any possible long-lived neutron star remnant in GW170817.

We fit both analytic and hydrodynamical models to the nonthermal afterglow to estimate the physical, geometrical, and microphysical parameters associated with the jet. These parameters are tabulated in Table 4. We find that the ratio of the jet energy to the ISM density, E/n_{ISM} , is $\mathcal{O}(52)$ – $\mathcal{O}(53)$. The jet opening angle is a few degrees for all of the models. The best-fit viewing angle is calculated to be $\simeq 15^\circ$ using analytical models that include the VLBI proper-motion constraint, but $\simeq 35^\circ$ when using a structured jet model that does not attempt to fit the VLBI proper-motion constraint. These viewing angle estimates lie at the tail end of the values previously published.

The wide range of viewing angles θ_v , seemingly inconsistent within uncertainties (see Table 5) obtained using different modeling techniques (used here and in previous studies), can be explained through the fitting of the VLBI proper-motion measurement (Mooley et al. 2018a) and the systematic uncertainties (which may not be quantifiable) associated with the models/simulations. Fitting of the VLBI proper motion is especially important since the viewing angle cannot be estimated accurately by the light curve alone. As long as $\theta_j < \theta_v \ll 1$, the light curve depends only on the ratio θ_v/θ_j and not on θ_v or θ_j alone. Once the proper-motion measurement is taken into account, it breaks the degeneracy and θ_v can be constrained (Mooley et al. 2018a, 2018b; Nakar 2020). We highlight the importance of considering these limitations when drawing any physical conclusions or comparing the modeling results obtained using different techniques.

Given the upper limit on the ISM density, $\lesssim 0.01 \text{ cm}^{-3}$ (Section 4), we predict that the radio emission arising from the dynamical ejecta (kilonova ejecta) can be detected in the future (Nakar & Piran 2011; Alexander et al. 2017; Radice et al. 2018; Hajela et al. 2019; Kathirgamaraju et al. 2019), depending on the actual ISM density and the velocity distribution of the ejecta. The latter is quite sensitive to the neutron equation of

state (EOS; e.g., Hotokezaka et al. 2018; Radice et al. 2018). For example, a soft EOS predicts a radio remnant with a flux density at a $\sim 10 \mu\text{Jy}$ level on a timescale of 10 yr, if the ISM density is $\sim 10^{-3} \text{ cm}^{-3}$ (Radice et al. 2018). Detecting a long-lasting radio remnant will offer an opportunity to constrain the neutron star EOS from the light curve.
































The authors thank Eleonora Troja and Brendan Connor for advice on the X-ray data analysis and are grateful to Schuyler van Dyk for helpful discussions on HST data. The MeerKAT telescope is operated by the South African Radio Astronomy Observatory, which is a facility of the National Research Foundation, an agency of the Department of Science and Innovation. The National Radio Astronomy Observatory is a facility of the National Science Foundation operated under cooperative agreement by Associated Universities, Inc. The authors thank the NRAO staff, especially Mark Claussen and Amy Mioduszewski, for scheduling the VLA observations. The Australia Telescope is funded by the Commonwealth of Australia for operation as a National Facility managed by CSIRO. We acknowledge the Gomeroi people as the traditional owners of the Observatory site. We thank the staff of the GMRT that made these observations possible. GMRT is run by the National Centre for Radio Astrophysics of the Tata Institute of Fundamental Research. The MeerKAT telescope is operated by the South African Radio Astronomy Observatory, (SARAO), which is a facility of the National Research Foundation (NRF), an agency of the Department of Science and Technology. K.P.M. is a Jansky Fellow of the National Radio Astronomy Observatory. K.P.M. and G.H. acknowledge support from the National Science Foundation Grant AST-1911199. D.D. is supported by an Australian Government Research Training Program Scholarship. T.M. acknowledges the support of the Australian Research Council through grant DP190100561. Parts of this research were conducted by the Australian Research Council Centre of Excellence for Gravitational Wave Discovery (OzGrav), project number CE170100004. We acknowledge support by the GROWTH (Global Relay of Observatories Watching Transients Happen) project funded by the National Science Foundation PIRE (Partnership in International Research and Education) program under grant No. 1545949. D.L. acknowledges support

from NASA grants 80NSSC18K1729 (Fermi) and NNX17AK42G (ATP), Chandra grant TM9-20002X, and NSF grant AST-1907955. This research has made use of NASA's Astrophysics Data System Bibliographic Services. C.F. gratefully acknowledges support of his research by the Heising-Simons Foundation. JM acknowledges financial support from the State Agency for Research of the Spanish MCIU through the "Center of Excellence Severo Ochoa" award to the Instituto de Astrofísica de Andalucía (SEV-2017-0709) and from the grant RTI2018-096228-B-C31 (MICIU/FEDER, EU). D.L.K. was supported by NSF grant AST-1816492. P.K. is partially supported by the BMBF project 05A17PC2for D-MeerKAT. A.B. and A.C. acknowledge support from the National Science Foundation via grant #1907975.

Facilities: VLA, ATCA, uGMRT, MeerKAT, eMERLIN, HST, Chandra, XMM-Newton.

Software: MIRIAD (Sault et al. 1995), CASA (McMullin et al. 2007, release 5.6.2-3.el7), emcee (Foreman-Mackey et al. 2013), corner (Foreman-Mackey 2016), CARACal (Ramatsoku et al. 2020, beta version), AOFlagger (Offringa et al. 2010, version 2.14.0), WSClean (Offringa et al. 2014, version 2.8.0), CubiCal (Kenyon et al. 2018, version 1.2.2), MeqTrees (Noordam & Smirnov 2010, version 1.6.0).

ORCID iDs

S. Makhathini  <https://orcid.org/0000-0001-9565-9622>
 K. P. Mooley  <https://orcid.org/0000-0002-2557-5180>
 M. Brightman  <https://orcid.org/0000-0002-8147-2602>
 K. Hotokezaka  <https://orcid.org/0000-0002-2502-3730>
 H. T. Intema  <https://orcid.org/0000-0002-5880-2730>
 D. Dobie  <https://orcid.org/0000-0003-0699-7019>
 E. Lenc  <https://orcid.org/0000-0002-9994-1593>
 D. A. Perley  <https://orcid.org/0000-0001-8472-1996>
 C. Fremling  <https://orcid.org/0000-0002-4223-103X>
 J. Moldòn  <https://orcid.org/0000-0002-8079-7608>
 D. Lazzati  <https://orcid.org/0000-0002-9190-662X>
 D. L. Kaplan  <https://orcid.org/0000-0001-6295-2881>
 D. Carbone  <https://orcid.org/0000-0002-6575-4642>
 P. Chandra  <https://orcid.org/0000-0002-0844-6563>
 A. Corsi  <https://orcid.org/0000-0001-8104-3536>
 F. Camilo  <https://orcid.org/0000-0002-1873-3718>
 A. Deller  <https://orcid.org/0000-0001-9434-3837>
 T. Murphy  <https://orcid.org/0000-0002-2686-438X>
 E. J. Murphy  <https://orcid.org/0000-0001-7089-7325>
 E. Nakar  <https://orcid.org/0000-0002-4534-7089>
 O. Smirnov  <https://orcid.org/0000-0003-1680-7936>
 R. J. Beswick  <https://orcid.org/0000-0002-5544-2354>
 G. Hallinan  <https://orcid.org/0000-0002-7083-4049>
 M. Kasliwal  <https://orcid.org/0000-0002-5619-4938>
 B. Lee  <https://orcid.org/0000-0003-1954-5046>
 W. Lu  <https://orcid.org/0000-0002-1568-7461>
 J. Rana  <https://orcid.org/0000-0001-5605-1809>
 S. Perkins  <https://orcid.org/0000-0002-3623-0938>
 S. V. White  <https://orcid.org/0000-0002-2340-8303>
 G. I. G. Józsa  <https://orcid.org/0000-0003-0608-6258>
 P. Kamphuis  <https://orcid.org/0000-0002-5425-6074>

References

Abbott, B. P., Abbott, R., Abbott, T. D., et al. 2017a, *PhRvL*, **118**, 221101
 Abbott, B. P., Abbott, R., Abbott, T. D., et al. 2017b, *ApJL*, **848**, L12
 Alexander, K. D., Berger, E., Fong, W., et al. 2017, *ApJL*, **848**, L21
 Alexander, K. D., Margutti, R., Blanchard, P. K., et al. 2018, *ApJL*, **863**, L18

Arcavi, I., Hosseinzadeh, G., Howell, D. A., et al. 2017, *Natur*, **551**, 64
 Asad, K. M. B., Girard, J. N., deVilliers, M., et al. 2021, *MNRAS*, **502**, 2970
 Babyk, I. V., McNamara, B. R., Nulsen, P. E. J., et al. 2018, *ApJ*, **857**, 32
 Bertin, E., & Arnouts, S. 1996, *A&AS*, **117**, 393
 Blandford, R. D., & McKee, C. F. 1976, *BAAS*, **8**, 539
 Broderick, J. W., Shimwell, T. W., Gourdji, K., et al. 2020, *MNRAS*, **494**, 5110
 Camilo, F., Scholz, P., Serylak, M., et al. 2018, *ApJ*, **856**, 180
 Cavaliere, A., & Fusco-Femiano, R. 1978, *A&A*, **70**, 677
 Chandra, P., & Kanekar, N. 2017, *ApJ*, **846**, 111
 Corsi, A., Hallinan, G. W., Lazzati, D., et al. 2018, *ApJL*, **861**, L10
 Coulter, D. A., Foley, R. J., Kilpatrick, C. D., et al. 2017, *Sci*, **358**, 1556
 Cowperthwaite, P. S., Berger, E., Villar, V. A., et al. 2017, *ApJL*, **848**, L17
 D'Avanzo, P., Campana, S., Salafia, O. S., et al. 2018, *A&A*, **613**, L1
 Dobie, D., Kaplan, D. L., Murphy, T., et al. 2018, *ApJL*, **858**, L15
 Drout, M. R., Piro, A. L., Shappee, B. J., et al. 2017, *Sci*, **358**, 1570
 Evans, P. A., Cenke, S. B., Kennea, J. A., et al. 2017, *Sci*, **358**, 1565
 Fong, W., Berger, E., Margutti, R., & Zauderer, B. A. 2015, *ApJ*, **815**, 102
 Fong, W., Blanchard, P. K., Alexander, K. D., et al. 2019, *ApJL*, **883**, L1
 Foreman-Mackey, D. 2016, *JOSS*, **1**, 24
 Foreman-Mackey, D., Hogg, D. W., Lang, D., & Goodman, J. 2013, *PASP*, **125**, 306
 Fruscione, A., McDowell, J. C., Allen, G. E., et al. 2006, *Proc. SPIE*, **6270**, 62701V
 Fryxell, B., Olson, K., Ricker, P., et al. 2000, *ApJS*, **131**, 273
 Garrington, S. T., Anderson, B., Baines, C., et al. 2004, *Proc. SPIE*, **5489**, 332
 Ghirlanda, G., Salafia, O. S., Paragi, Z., et al. 2019, *Sci*, **363**, 968
 Giacomazzo, B., Zrake, J., Duffell, P. C., MacFadyen, A. I., & Perna, R. 2015, *ApJ*, **809**, 39
 Gill, R., & Granot, J. 2018, *MNRAS*, **478**, 4128
 Goldstein, A., Veres, P., Burns, E., et al. 2017, *ApJL*, **848**, L14
 Gottlieb, O., Nakar, E., & Piran, T. 2018, *MNRAS*, **473**, 576
 Haggard, D., Nynka, M., Ruan, J. J., et al. 2017, *ApJL*, **848**, L25
 Hajela, A., Margutti, R., Alexander, K. D., et al. 2019, *ApJL*, **886**, L17
 Hajela, A., Margutti, R., Laskar, T., et al. 2020, *GCN*, **27414**, 1
 Hajela, A., Margutti, R., & Bright, J. S. 2021, arXiv:2104.02070
 Hallinan, G., Corsi, A., Mooley, K. P., et al. 2017, *Sci*, **358**, 1579
 HI4PI Collaboration, Ben Bekhti, N., Flöer, L., et al. 2016, *A&A*, **594**, A116
 Hotokezaka, K., Kashiyama, K., & Murase, K. 2017, *ApJ*, **850**, 18
 Hotokezaka, K., Kiuchi, K., Shibata, M., Nakar, E., & Piran, T. 2018, *ApJ*, **867**, 95
 Hotokezaka, K., Nakar, E., Gottlieb, O., et al. 2019, *NatAs*, **3**, 940
 Intema, H. T., Jagannathan, P., Mooley, K. P., & Frail, D. A. 2017, *A&A*, **598**, A78
 Intema, H. T., van der Tol, S., Cotton, W. D., et al. 2009, *A&A*, **501**, 1185
 Jonas, J. & (MeerKAT Team) 2018, in MeerKAT Science: On the Pathway to the SKA (MeerKAT2016) (Trieste: PoS)
 Kasen, D., Metzger, B., Barnes, J., Quataert, E., & Ramirez-Ruiz, E. 2017, *Natur*, **551**, 80
 Kasliwal, M. M., Nakar, E., Singer, L. P., et al. 2017, *Sci*, **358**, 1559
 Kathirgamaraju, A., Giannios, D., & Beniamini, P. 2019, *MNRAS*, **487**, 3914
 Kenyon, J. S., Smirnov, O. M., Grobler, T. L., & Perkins, S. J. 2018, *MNRAS*, **478**, 2399
 Kim, S., Schulze, S., Resmi, L., et al. 2017, *ApJL*, **850**, L21
 Kiuchi, K., Kyutoku, K., Sekiguchi, Y., Shibata, M., & Wada, T. 2014, *PhRvD*, **90**, 041502
 Lamb, G. P., Lyman, J. D., Levan, A. J., et al. 2019, *ApJL*, **870**, L15
 Lamb, G. P., Mandel, I., & Resmi, L. 2018, *MNRAS*, **481**, 2581
 Lazzati, D., López-Cámara, D., Cantiello, M., et al. 2017, *ApJL*, **848**, L6
 Lazzati, D., Perna, R., Morsony, B. J., et al. 2018, *PhRvL*, **120**, 241103
 Lyman, J. D., Lamb, G. P., Levan, A. J., et al. 2018, *NatAs*, **2**, 751
 Margutti, R., Alexander, K. D., Xie, X., et al. 2018, *ApJL*, **856**, L18
 Margutti, R., Berger, E., Fong, W., et al. 2017, *ApJL*, **848**, L20
 McMullin, J. P., Waters, B., Schiebel, D., Young, W., & Golap, K. 2007, in ASP Conf. Ser. 376, CASA Architecture and Applications, ed. R. A. Shaw, F. Hill, & D. J. Bell (San Francisco, CA: ASP), **127**
 Metzger, B. D. 2017, arXiv:1710.05931
 Mohan, N., & Rafferty, D. 2015, PyBDSF: Python Blob Detection and Source Finder, Astrophysics Source Code Library, ascl:1502.007
 Mooley, K. P., Deller, A. T., Gottlieb, O., et al. 2018a, *Natur*, **561**, 355
 Mooley, K. P., Frail, D. A., Dobie, D., et al. 2018b, *ApJL*, **868**, L11
 Mooley, K. P., Nakar, E., Hotokezaka, K., et al. 2018c, *Natur*, **554**, 207
 Murguia-Berthier, A., Ramirez-Ruiz, E., Kilpatrick, C. D., et al. 2017, *ApJL*, **848**, L34
 Muxlow, T. W. B., Thomson, A. P., Radcliffe, J. F., et al. 2020, *MNRAS*, **495**, 1188
 Nakar, E. 2020, *PhR*, **886**, 1

- Nakar, E., Gottlieb, O., Piran, T., Kasliwal, M. M., & Hallinan, G. 2018, *ApJ*, **867**, 18
- Nakar, E., & Piran, T. 2011, *Natur*, **478**, 82
- Nakar, E., & Piran, T. 2018, *MNRAS*, **478**, 407
- Nicholl, M., Berger, E., Kasen, D., et al. 2017, *ApJL*, **848**, L18
- Noordam, J. E., & Smirnov, O. M. 2010, *A&A*, **524**, A61
- Nynka, M., Ruan, J. J., Haggard, D., & Evans, P. A. 2018, *ApJL*, **862**, L19
- Offringa, A. R., de Bruyn, A. G., Zaroubi, S., & Biehl, M. 2010, arXiv:1007.2089
- Offringa, A. R., McKinley, B., Hurley-Walker, N., et al. 2014, *MNRAS*, **444**, 606
- Pan, Y. C., Kilpatrick, C. D., Simon, J. D., et al. 2017, *ApJL*, **848**, L30
- Partridge, B., López-Caniego, M., Perley, R. A., et al. 2016, *ApJ*, **821**, 61
- Pearson, T. J., & Readhead, A. C. S. 1984, *ARA&A*, **22**, 97
- Peng, C. Y., Ho, L. C., Impey, C. D., & Rix, H.-W. 2002, *AJ*, **124**, 266
- Perley, R. A., & Butler, B. J. 2017, *ApJS*, **230**, 7
- Pian, E., D'Avanzo, P., Benetti, S., et al. 2017, *Natur*, **551**, 67
- Piro, L., Troja, E., Zhang, B., et al. 2019, *MNRAS*, **483**, 1912
- Pooley, D., Kumar, P., Wheeler, J. C., & Grossan, B. 2018, *ApJL*, **859**, L23
- Radice, D., Perego, A., Hotokezaka, K., et al. 2018, *ApJ*, **869**, 130
- Ramatsoku, M., Murgia, M., Vacca, V., et al. 2020, *A&A*, **636**, L1
- Resmi, L., Schulze, S., Ishwara-Chandra, C. H., et al. 2018, *ApJ*, **867**, 57
- Ruan, J. J., Nynka, M., Haggard, D., Kalogera, V., & Evans, P. 2018, *ApJL*, **859**, L16
- Ryan, G., van Eerten, H., Piro, L., & Troja, E. 2020, *ApJ*, **896**, 166
- Sault, R. J., Teuben, P. J., & Wright, M. C. H. 1995, in ASP Conf. Ser. 77, A Retrospective View of MIRIAD, ed. R. A. Shaw, H. E. Payne, & J. J. E. Hayes (San Francisco, CA: ASP), 433
- Savchenko, V., Ferrigno, C., Kuulkers, E., et al. 2017, *ApJL*, **848**, L15
- Shepherd, M. C. 1997, in ASP Conf. Ser. 125, Difmap: an Interactive Program for Synthesis Imaging, ed. G. Hunt & H. Payne (San Francisco, CA: ASP), 77
- Smartt, S. J., Chen, T. W., Jerkstrand, A., et al. 2017, *Natur*, **551**, 75
- Soares-Santos, M., Holz, D. E., Annis, J., et al. 2017, *ApJL*, **848**, L16
- Spitkovsky, A. 2006, *ApJL*, **648**, L51
- Tanvir, N. R., Levan, A. J., González-Fernández, C., et al. 2017, *ApJL*, **848**, L27
- Troja, E., O'Connor, B., Ryan, G., et al. 2021, arXiv:2104.13378
- Troja, E., Piro, L., Ryan, G., et al. 2018, *MNRAS*, **478**, L18
- Troja, E., Piro, L., van Eerten, H., et al. 2017, *Natur*, **551**, 71
- Troja, E., van Eerten, H., Ryan, G., et al. 2019, *MNRAS*, **489**, 1919
- Troja, E., van Eerten, H., Zhang, B., et al. 2020, *MNRAS*, **498**, 5643
- Valenti, S., Sand, D. J., Yang, S., et al. 2017, *ApJL*, **848**, L24
- van Eerten, H., & MacFadyen, A. 2013, *ApJ*, **767**, 141
- Villar, V. A., Guillochon, J., Berger, E., et al. 2017, *ApJL*, **851**, L21
- Wu, Y., & MacFadyen, A. 2019, *ApJL*, **880**, L23
- Yu, Y.-W., Liu, L.-D., & Dai, Z.-G. 2018, *ApJ*, **861**, 114
- Zrake, J., & MacFadyen, A. I. 2013, *ApJL*, **769**, L29